Computer Assisted Mechanics and Engineering Sciences, 4: 27–54, 1997.

Robustness in numerical computations of damage evolution in cohesive-frictional materials

René de Borst
Delft University of Technology, Faculty of Civil Engineering/
Eindhoven University of Technology, Faculty of Mechanical Engineering
P.O. Box 5048, NL-2600 GA Delft, The Netherlands

(Received May 27, 1996)

Numerical simulations of the mechanical behaviour of structures composed of cohesive-frictional materials such as soils, concrete and rocks, still suffer from a lack of robustness. Too often an inability to continue the computation beyond a certain level of loading is encountered. Also, predictions of the structural behaviour can be quite inaccurate, with errors amounting up to 100%. Some typical causes for these observations are discussed and some remedies are suggested.

1. Introduction

Since the early use of computers for structural analysis in the 1950s, a continuous improvement has been observed in the ability of software to simulate the behaviour of structures and structural components. Concentrating on the finite element method, the initial focus on linear elastic material behaviour was extended to geometrically and physically nonlinear behaviour in the late 1960s and early 1970s. Indeed, successful computations have already been reported some twenty-five years ago, especially for metals, where geometric nonlinearity and relatively simple plasticity models suffice to describe many of the essential features.

Computations appeared far more complicated when endeavours were made to obtain accurate numerical solutions for failure of structures and structural components. This already holds true when metals are considered. For structures composed of cohesive-frictional materials (soils, concrete, rocks, ceramics, powders), the difficulties encountered seemed almost insurmountable because of typical features like friction, non-associated plasticity, cracking and softening.

Herein, we shall make a modest attempt to categorise these difficulties. Of course, such a categorisation is by nature deficient. In the present case, it simply reflects some of the author's experiences with difficulties he has encountered in the numerical modelling of these materials and structures.

2. An overview

A crucial step for any prediction of structural behaviour is the choice of the constitutive model for the material behaviour. Here, two potential pitfalls exist. Firstly, there is the requirement of proper constitutive modelling, in the sense that for elementary tests the material response should be simulated closely. Secondly, the constitutive equations together with the kinematic equations, the equations of motion and the appropriate boundary conditions should result in a rate boundary value problem that is well-posed. Let us suppose that we have a constitutive model that satisfies both above listed requirements. Then, the issue arises of a proper discretisation of the rate boundary value problem. This can again be a source of errors and difficulties, not in the least because many discretisations that perform well for linear systems, can behave poorly for nonlinear applications. Locking of elements for constrained media and spurious mechanisms induced by

material nonlinearities are prime examples. Finally, even if the constitutive model and the adopted numerical methodology are sound, the analyst can arrive at answers that are far from the physical reality. In particular the boundary conditions that have to be modelled are often quite problematic for complex structures. Improper assumptions can cause deviations in the structural response that easily amount to more than 100%.

We have structured this contribution as follows. Firstly, we shall discuss an example of how constitutive modelling can affect the outcome of an analysis. Concrete cracking will be considered and elementary examples will be treated subject to nonproportional loading paths of biaxial tension and shear. Then, a succinct review will be presented of the ill-posedness that results when a straightforward smeared crack model for concrete or rock is adopted in the constitutive modelling. In the next section, a simple linear-elastic, perfectly plastic soil model will be adopted to show the possible shortcomings and instabilities of commonly used finite elements. Finally, we shall treat the collapse analysis of a real reinforced concrete three-way bridge slab. This analysis clearly demonstrates the need for a good engineering estimate of the appropriate boundary conditions.

3. Deficiencies in the constitutive models: smeared cracking

The success of accurate predictions of the direction of crack propagation in smeared-crack finite element representations depends to a large extent on the tangential shear stiffness of the constitutive relation. A large number of constitutive models have been proposed in the past, which lead to different predictions for the incremental shear stiffness. Sometimes these differences are large, sometimes they are hardly discernible, which is related to the similarity of some of the fracture formulations.

A possible way to categorise crack models is to divide them into models that are based on a total formulation, i.e. there exists an injective relation between the total stresses and the total strains, and models that employ a linear relation between stress rate and strain rate via a loading history dependent tangential modulus. Examples of the former category are the elasticity-based fixed crack model, the rotating crack model [12], a deformation plasticity theory with a Rankine type yield locus [14] and elasticity-based damage models, either isotropic [19] or anisotropic [18]. In the second class of models we have the multidirectional crack model [8–10, 21] and the Rankine plasticity model based on a flow theory of plasticity [14]. Although major conceptual differences underly the various formulations, remarkable similarities exist especially between plasticity-based models and the familiar rotating crack model when typical non-proportional load paths are simulated. On the other hand the classical fixed crack model gives predictions that significantly differ from most of the other approaches, in the sense that the model usually responds too stiff.

3.1. A categorisation of smeared-crack models

Limiting the discussion to grade-1 materials a total stress-strain relation can be defined as

$$\boldsymbol{\varepsilon} = f(\boldsymbol{\sigma}, \boldsymbol{\eta}, \kappa)\,, \tag{1}$$

with f a tensor-valued function, $\boldsymbol{\varepsilon}$ a strain tensor, $\boldsymbol{\sigma}$ a stress tensor, and $\boldsymbol{\eta}$ and κ tensor and scalar-valued internal variables, which reflect the loading history of the material element. Eq. (1) assumes the existence of a single tensor-valued internal variable, $\boldsymbol{\eta}$, and a single scalar valued internal variable, κ. Extension of this formulation to include more such variables poses no fundamental problem, but is not necessary for our present purpose. Alternatively, a constitutive formulation can be phrased in rate format, such that

$$\dot{\boldsymbol{\varepsilon}} = f(\boldsymbol{\sigma}, \dot{\boldsymbol{\sigma}}, \boldsymbol{\eta}, \kappa)\,, \tag{2}$$

whereby the dots signify differentiation with respect to a virtual time. A subclass of constitutive models that fits within the framework of Eq. (2) are the incrementally-linear models,

$$\dot{\boldsymbol{\varepsilon}} = \mathbf{C}(\boldsymbol{\sigma}, \boldsymbol{\eta}, \kappa)\dot{\boldsymbol{\sigma}}\,, \tag{3}$$

with $\mathbf{C}$ a tangential compliance tensor.

A simple model that falls into category (3) is elasticity: $\boldsymbol{\varepsilon} = f(\boldsymbol{\sigma})$, which for linear elasticity reduces to $\boldsymbol{\varepsilon} = \mathbf{C}^{\mathrm{e}}\boldsymbol{\sigma}$, with $\mathbf{C}^{\mathrm{e}}$ the fourth-order elastic compliance tensor with E the Young's modulus and the Poisson's ratio ν as constants for the isotropic case. History dependence can be incorporated in a simple manner by degrading the elastic compliance via a scalar-valued internal parameter ω:

$$\boldsymbol{\varepsilon} = \frac{\mathbf{C}^{\mathrm{e}}\boldsymbol{\sigma}}{1-\omega}\,. \tag{4}$$

or with $\mathbf{D}^{\mathrm{e}} = [\mathbf{C}^{\mathrm{e}}]^{-1}$,

$$\boldsymbol{\sigma} = (1-\omega)\mathbf{D}^{\mathrm{e}}\boldsymbol{\varepsilon}\,. \tag{5}$$

In this isotropic elasticity-based damage theory the damage variable ω grows from zero to one (complete loss of integrity). Damage growth is possible if the damage loading function

$$f(\tilde{\varepsilon}, \kappa) = \tilde{\varepsilon} - \kappa \tag{6}$$

vanishes. In particular, the damage loading function f and the rate of damage growth $\dot{\omega}$ have to satisfy the discrete Kuhn-Tucker conditions

$$f \leq 0\,, \quad \dot{\omega} \geq 0\,, \quad f\dot{\omega} = 0\,. \tag{7}$$

In (6) $\tilde{\varepsilon}$ is the equivalent strain, which can be a function of the strain invariants, the principal strains as in Reference [19]

$$\tilde{\varepsilon} = \sqrt{\sum_{i=1}^{3} \left(\langle \varepsilon_i \rangle\right)^2}\,, \tag{8}$$

with ε_i the principal strains, and $\langle \varepsilon_i \rangle = \varepsilon_i$ if $\varepsilon_i > 0$ and $\langle \varepsilon_i \rangle = 0$ otherwise, or the local energy release due to damage

$$\tilde{\varepsilon} = \tfrac{1}{2}\boldsymbol{\varepsilon}^{\mathrm{T}}\mathbf{C}^{\mathrm{e}}\boldsymbol{\varepsilon}\,. \tag{9}$$

The parameter κ starts at a damage threshold level κ_0 and is updated by the requirement that during damage growth $f = 0$. Damage growth occurs according to an evolution law $F(\tilde{\varepsilon})$ such that

$$\omega = F(\tilde{\varepsilon}) \tag{10}$$

Isotropic damage models have been used successfully in predictions of crack propagation in plain and reinforced concrete [19]. The disadvantage of an isotropic damage model is that possible compressive strut action is eliminated. This is a disadvantage particularly for the analysis of reinforced concrete structures.

Directional dependence of damage evolution can be incorporated by degrading the Young's modulus E in the direction of the major principal stress only. When, for planar conditions, distinction is made between the global x, y-coordinate system and a local n, s-coordinate system aligned with the principal stress axes one obtains in the local coordinate system the secant tangential stiffness relation

$$\boldsymbol{\sigma}_{\mathrm{ns}} = {}^{\mathrm{s}}\mathbf{D}_{\mathrm{ns}}\boldsymbol{\varepsilon}_{\mathrm{ns}} \tag{11}$$

with ${}^{\mathrm{s}}\mathbf{D}_{\mathrm{ns}}$ defined as

$$ {}^{\mathrm{s}}\mathbf{D}_{\mathrm{ns}} = \begin{bmatrix} (1-\omega)E & 0 & 0 \\ 0 & E & 0 \\ 0 & 0 & \beta G \end{bmatrix} , \tag{12} $$

with $\omega = \omega(\varepsilon_{nn})$ and $\beta = \beta(\varepsilon_{nn})$ functions of the normal strain in the local n-direction. The (secant) shear reduction factor β represents the degradation of the elastic stiffness G and is gradually reduced from one to zero. Alternatively, β can be assigned a constant value between zero and one. In a further enhancement Poisson coupling can be added in the secant stiffness relation of the damaged material [14].

Let now ϕ be the angle between the n and x axes and assume that the directions of principal stress and strain coincide throughout the damage process. Then, the standard tranformation rules for second order tensors apply:

$$ \boldsymbol{\varepsilon}_{\mathrm{ns}} = \mathbf{T}(\phi)\boldsymbol{\varepsilon}_{\mathrm{xy}} \tag{13} $$

and

$$ \boldsymbol{\sigma}_{\mathrm{ns}} = \mathbf{T}(\phi)\boldsymbol{\sigma}_{\mathrm{xy}} \tag{14} $$

with $\mathbf{T}$ the standard transformation matrix. Combination of Eqs. (11), (13) and (14) yields

$$ \boldsymbol{\sigma}_{\mathrm{xy}} = \mathbf{T}^{\mathrm{T}}(\phi)\ {}^{\mathrm{s}}\mathbf{D}_{\mathrm{ns}}\ \mathbf{T}(\phi)\,\boldsymbol{\varepsilon}_{\mathrm{xy}} . \tag{15} $$

Equation (15) incorporates the traditional fixed crack model and the rotating crack model. The only difference is that in the fixed crack model the inclination angle ϕ is fixed when the major principal stress first exceeds the tensile strength ($\phi = \phi_0$), while in the rotating crack concept ϕ changes such that the n-axis continues to coincide with the major principal stress direction. This difference has profound consequences when deriving the tangential stiffness, especially with regard to the shear term. For the fixed crack model differentiation of Eq. (15) yields

$$ \dot{\boldsymbol{\sigma}}_{\mathrm{xy}} = \mathbf{T}^{\mathrm{T}}(\phi_0)\ \mathbf{D}_{\mathrm{ns}}\ \mathbf{T}(\phi_0)\,\dot{\boldsymbol{\varepsilon}}_{\mathrm{xy}} \tag{16} $$

with $\mathbf{D}_{\mathrm{ns}}$ the local material tangential stiffness matrix:

$$ \mathbf{D}_{\mathrm{ns}} = \begin{bmatrix} (1-\omega-\omega'\varepsilon_{nn})E & 0 & 0 \\ 0 & E & 0 \\ \beta'\gamma_{ns}G & 0 & \beta G \end{bmatrix} , \tag{17} $$

where the prime signifies differentiation with respect to ε_{nn}. From Eq. (17) we observe that for non-constant β the local material tangential stiffness matrix becomes non-symmetric. On the other hand, the requirement of coaxiality between stress and strain tensors that is imposed in the rotating crack model results in a considerably more complicated expression [3, 21, 28]:

$$ \dot{\boldsymbol{\sigma}}_{\mathrm{xy}} = \left[\mathbf{T}^{\mathrm{T}}(\phi_0)\ \mathbf{D}_{\mathrm{ns}}\ (\mathbf{I}-\mathbf{L})\mathbf{T}(\phi_0) + \alpha\mathbf{T}^{\mathrm{T}}(\phi_0)\ \mathbf{L}\ \mathbf{T}(\phi_0)\right]\ \dot{\boldsymbol{\varepsilon}}_{\mathrm{xy}} \tag{18} $$

with $\mathbf{I}$ the identity matrix, $\mathbf{L} = \mathrm{diag}[0, 0, -1]$, and $\alpha = (\sigma_{nn} - \sigma_{ss})/[2(\varepsilon_{nn} - \varepsilon_{ss})]$. Comparison of (16) and (18) shows that the *tangential* shear stiffness is now given by α instead of βG. As we shall show in the example to be discussed in the next paragraph α can become negative, leading to a reduction of existing shear stresses and thereby also reducing the existence of locked-in stresses [21].

In all formulations discussed above the strains were recoverable. Upon removal of the load the strains vanish. This is not so for a deformation type plasticity model, which can also be cast in the format (1). In it the total strain is partitioned into an elastic part $\boldsymbol{\varepsilon}^{\mathrm{e}}$ and an inelastic part $\boldsymbol{\varepsilon}^{\mathrm{i}}$, as follows

$$ \boldsymbol{\varepsilon} = \boldsymbol{\varepsilon}^{\mathrm{e}} + \boldsymbol{\varepsilon}^{\mathrm{i}} . \tag{19} $$

The elastic strains are related to the stresses via

$$\boldsymbol{\varepsilon}^{\mathrm{e}} = \mathbf{C}^{\mathrm{e}}\boldsymbol{\sigma}\,, \tag{20}$$

while the inelastic strains are derivable from a plastic potential f

$$\boldsymbol{\varepsilon}^{\mathrm{i}} = \lambda\frac{\partial f}{\partial \boldsymbol{\sigma}} \tag{21}$$

where the plastic multiplier λ and $f(\boldsymbol{\sigma}, \boldsymbol{\eta}, \kappa)$ must satisfy the discrete Kuhn-Tucker conditions $\lambda \geq 0$, $f \leq 0$ and $f\lambda = 0$. Accordingly, f also takes the role of a loading function. Combining Eqs. (19)–(21) results in

$$\boldsymbol{\varepsilon} = \mathbf{C}^{\mathrm{e}}\boldsymbol{\sigma} + \lambda\frac{\partial f}{\partial \boldsymbol{\sigma}} \tag{22}$$

which, upon elaboration, can be shown to fit the format (1).

We now select the Rankine (major principal stress) criterion as loading function and plastic potential and we introduce the reduced stress tensor $\boldsymbol{\xi} = \boldsymbol{\sigma} - \boldsymbol{\eta}$, with $\boldsymbol{\eta}$ the so-called back stress tensor, which governs the amount of kinematic hardening. In a plane-stress configuration the major principal stress can be expressed in terms of the stress vector with the aid of Mohr's circle and one obtains

$$f = \sqrt{\tfrac{1}{2}\boldsymbol{\xi}^{\mathrm{T}}\mathbf{P}\boldsymbol{\xi}} + \tfrac{1}{2}\boldsymbol{\pi}^{\mathrm{T}}\boldsymbol{\xi} - \bar{\sigma}(\gamma\kappa) \tag{23}$$

with the equivalent stress $\bar{\sigma}$ a function of the internal parameter κ, and γ a factor which sets the ratio between kinematic hardening/softening and isotropic hardening/softening. Pure kinematic hardening is obtained for $\gamma = 0$ and $\gamma = 1$ sets the other limiting case of pure isotropic hardening/softening. The projection matrix $\mathbf{P}$ and the projection vector $\boldsymbol{\pi}$ are given by

$$\mathbf{P} = \begin{bmatrix} \frac{1}{2} & -\frac{1}{2} & 0 \\ -\frac{1}{2} & \frac{1}{2} & 0 \\ 0 & 0 & 2 \end{bmatrix}, \tag{24}$$

and

$$\boldsymbol{\pi} = [1\,,\ 1\,,\ 0]^{\mathrm{T}}\,, \tag{25}$$

respectively. The equivalent stress $\bar{\sigma}(\gamma\kappa)$ is the current uniaxial tensile strength which starts at the initial tensile strength f_{t} and evolves for instance according to a tension-softening model with a fracture energy G_{f}. The internal parameter κ is assumed to be a measure for the internal damage and is supposed to be determined by a work-hardening hypothesis

$$\kappa\bar{\sigma} = \boldsymbol{\xi}^{\mathrm{T}}\boldsymbol{\varepsilon}^{\mathrm{i}}\,. \tag{26}$$

The back stress $\boldsymbol{\eta}$ is given by

$$\boldsymbol{\eta} = \lambda(1-\gamma)E_{\mathrm{ks}}\boldsymbol{\Lambda}\frac{\partial f}{\partial \boldsymbol{\sigma}} \tag{27}$$

with E_{ks} a secant stiffness modulus and $\boldsymbol{\Lambda} = \mathrm{diag}[1\,,\ 1\,,\ \frac{1}{2}]$. A rationale for this formulation has been given by Feenstra [14].

Alternatively, the Rankine yield criterion (23) can be used within the framework of a flow theory of plasticity. While the strain decomposition (19) and the relation for the elastic strains (20) remain unaffected, a direct expression for the inelastic strain in the sense of Eq. (21) is no longer assumed. Instead, an expression for the inelastic strain rate is adopted

$$\dot{\boldsymbol{\varepsilon}}^{\mathrm{i}} = \dot{\lambda}\frac{\partial f}{\partial \boldsymbol{\sigma}} \tag{28}$$

where the plastic flow rate $\dot{\lambda}$ must satisfy the Kuhn-Tucker conditions: $\dot{\lambda} \geq 0$, $f \leq 0$ and $f\dot{\lambda} = 0$. In a similar spirit we now have to define evolution equations for the rate of the internal hardening/softening parameter κ

$$\dot{\kappa}\bar{\sigma} = \boldsymbol{\xi}^{\mathrm{T}}\dot{\boldsymbol{\varepsilon}}^{\mathrm{i}} \tag{29}$$

and the back stress rate

$$\dot{\boldsymbol{\eta}} = \dot{\lambda}(1-\gamma)E_{\mathrm{ks}}\boldsymbol{\Lambda}\frac{\partial f}{\partial \boldsymbol{\sigma}}. \tag{30}$$

It is noted that differentiation of Eqs. (19)–(20) and combination with Eq. (28) results in

$$\dot{\boldsymbol{\varepsilon}} = \mathbf{C}^{\mathrm{e}}\dot{\boldsymbol{\sigma}} + \dot{\lambda}\frac{\partial f}{\partial \boldsymbol{\sigma}} \tag{31}$$

which, upon further elaboration can be shown to fall within the format (3).

3.2. An elementary tension-shear model problem

The fundamental differences of the formulations discussed so far will be elucidated with an elementary problem proposed by Willam *et al.* [28], in which a plane-stress element with unit dimensions is loaded in biaxial tension and shear. This causes a continuous rotation of the principal strain axes after cracking, as is typical of crack propagation in smeared crack finite element analysis. The element is subjected to tensile straining in the x-direction accompanied by lateral Poisson contraction in the y-direction to simulate uniaxial loading. Immediately after the tensile strength has been violated, the element is loaded in combined biaxial tension and shear strain, Figure 1. The ratio between the different strain components is given by $\Delta\varepsilon_{xx} : \Delta\varepsilon_{yy} : \Delta\gamma_{xy} = 0.5 : 0.75 : 1$. The reference set of material parameters is: Young's modulus $E = 10{,}000$ MPa, Poisson's ratio $\nu = 0.2$, tensile strength $f_{\mathrm{t}} = 1.0$ MPa. A linear strain softening diagram with a fracture energy $G_{\mathrm{f}} = 0.15 \times 10^{-3}$ N/mm has been used.

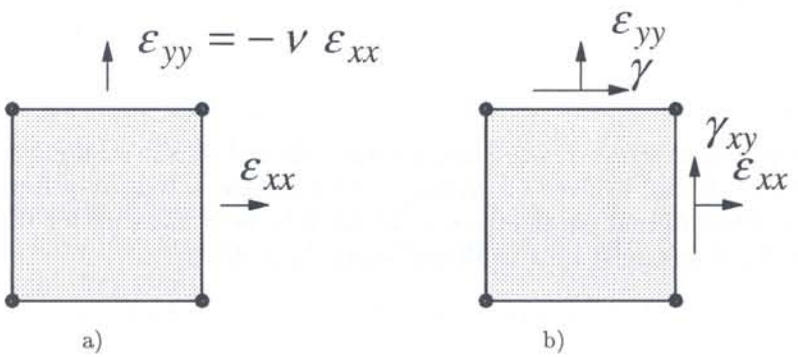

Fig. 1. Tension — shear model problem: a) tension up to cracking, b) biaxial tension with shear beyond cracking

The behaviour of the different formulations for smeared cracking can be studied in detail with this problem. The constitutive behaviour will be compared with respect to the shear stress–shear strain behaviour and the normal stress–normal strain behaviour in the x- and y-directions. Particularly the shear stress–shear strain response gives a good impression of the behaviour of the model when applied to the analyses of structures. The first issue which will be treated is the different behaviour of the models formulated in the total strain concept. The comparison between the isotropic damage model, the rotating crack model and the Rankine deformation plasticity model with isotropic and kinematic hardening should make clear whether the plasticity model is capable of predicting a flexible shear stress–shear strain response. The second issue is the comparison of the rotating crack model and the Rankine plasticity model within an incremental format. Because the response

of models with a total formulation is in general more flexible than the response of models with an incremental formulation, we expect that the Rankine plasticity model with an incremental formulation shows a less flexible shear stress–shear strain response, but the comparison should provide insight if this less flexible response is still acceptable.

The shear stress–shear strain response of the fixed and rotating crack models and the deformation theory based plasticity models is shown in Figures 2–4. The fixed crack model has been used

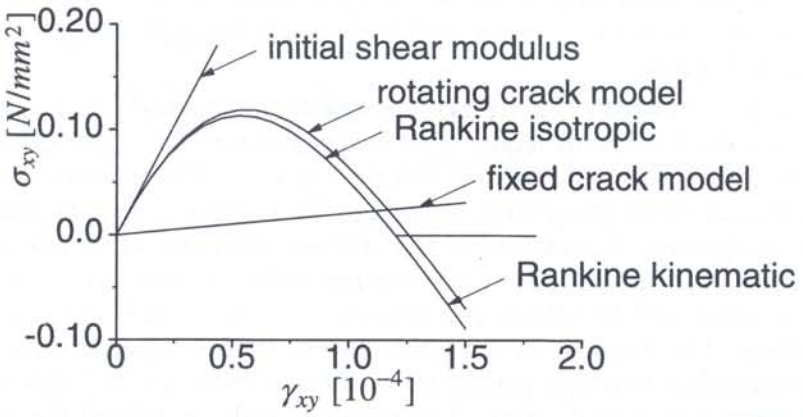

Fig. 2. Total formulation of the constitutive models. $\sigma_{xy} - \gamma_{xy}$ response.

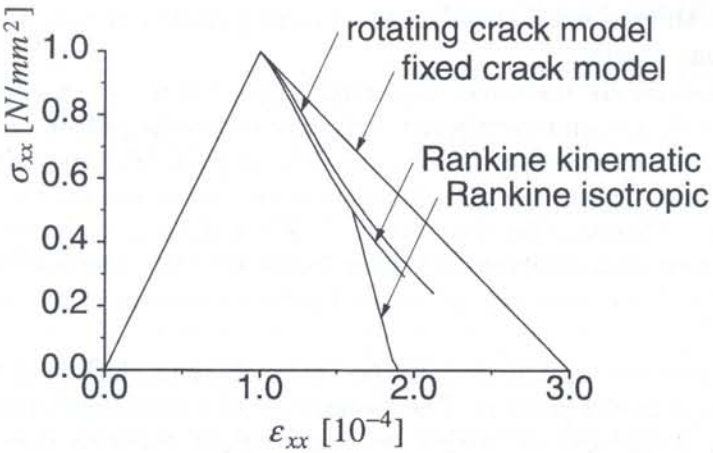

Fig. 3. Total formulation of the constitutive models. $\sigma_{xx} - \varepsilon_{xx}$ response.

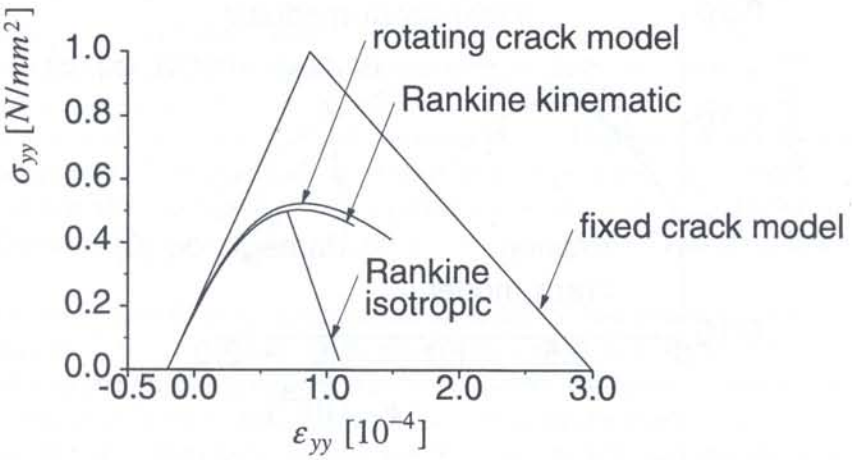

Fig. 4. Total formulation of the constitutive models. $\sigma_{yy} - \varepsilon_{yy}$ response.

with a shear reduction factor $\beta = 0.05$, which results in a monotonically increasing shear stress with increasing shear strain, Figure 2. The rotating crack model shows an implicit shear softening behaviour which has been observed previously [21, 28]. It is interesting that the same behaviour occurs for the deformation plasticity model either with isotropic or with kinematic hardening. The two formulations are in fact indiscernible until the shear stress has almost softened completely. Then the isotropic and the kinematic hardening models yield different responses which is due to the fact that with isotropic hardening it is impossible for the shear stress to become negative for positive increments of the shear strain component of the strain vector. It is obvious from Figure 2 that the differences with the rotating crack model are small, but that the fixed crack model gives a completely different response.

The σ_{xx}–ε_{xx} response depicted in Figure 3 shows that the input stress–strain softening diagram is exactly reproduced by the fixed crack model. This is logical, since the softening has been monitored in the fixed crack directions which are aligned with the x- y-axes. The behaviour of the other models shows an implicit normal stress–shear stress coupling. The Rankine plasticity model with isotropic softening shows a progressive degradation of the stiffness until the stress has been decreased to approximately 50% which is attended with a zero shear stress. At this stage the apex of the yield surface has been reached and the stress components in x and y-direction are softening in the direction of the origin. The response in the lateral y-direction is shown in Figure 4 which shows the formation of a secondary crack perpendicular to the first crack for the fixed crack model which again reflects the input softening diagram. The rotating crack model and the Rankine plasticity model with kinematic softening show a gradual degradation of the stiffness in the y-direction. This can also be observed for the Rankine plasticity model with isotropic softening until the shear stress becomes equal to zero and the stress in y-direction begins to soften linearly which is in accordance with the input softening diagram.

Although the tendencies are the same, somewhat larger differences exist between the rotating crack model and the deformation-type plasticity theories on one hand and, on the other hand, the isotropic damage models as formulated in Eqs. (5)–(10). In particular the shear stress response is stiffer, although to a lesser extent for the equivalent strain definition via the local energy release (Eq. (9)) than for that of Mazars (Eq. (8)), Figure 5. While the σ_{xx}–ε_{xx} curves are rather similar, Figure 6, the σ_{yy}–ε_{yy} responses displayed in Figure 7 show that here the isotropic softening models react much softer. The above observations are an inherent property of the isotropic character of the damage model.

The performance of the constitutive models based on a total formulation has been shown with the elementary tension-shear model problem. The formulation of a maximum principal stress criterion within the framework of elasticity or within the framework of plasticity does not result in major

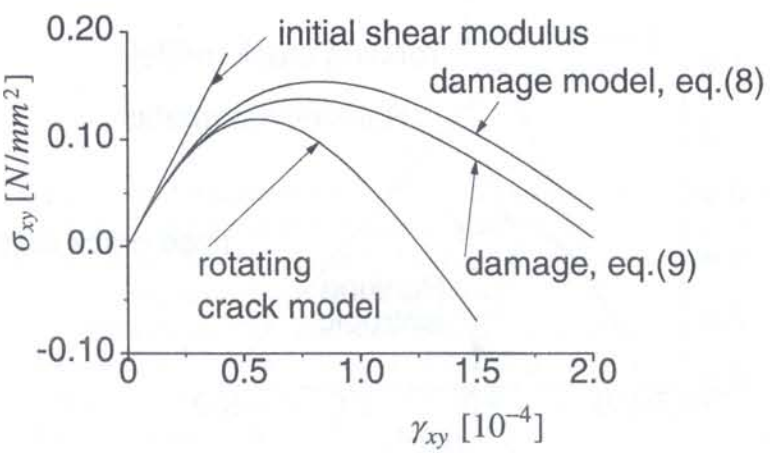

Fig. 5. Damage models and the rotating crack model. $\sigma_{xy} - \gamma_{xy}$ response.

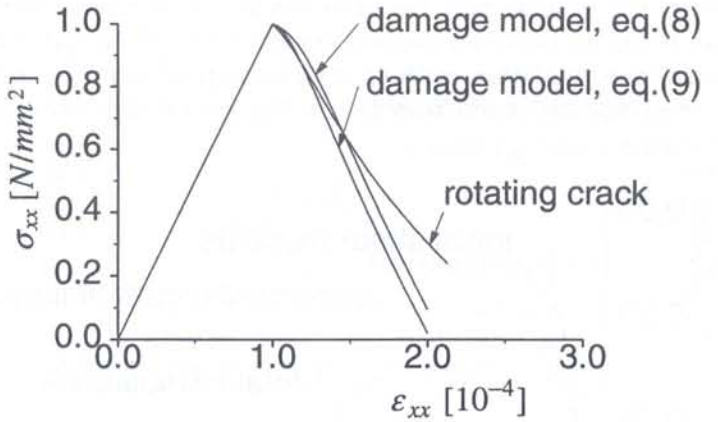

Fig. 6. Damage models and the rotating crack model. $\sigma_{xx} - \varepsilon_{xx}$ response.

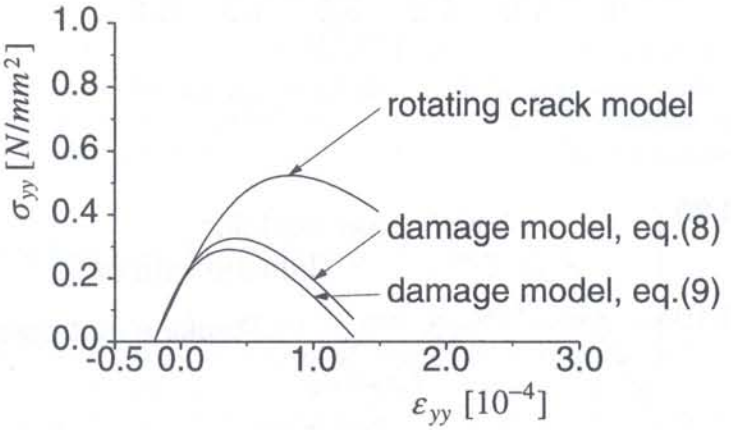

Fig. 7. Damage models and the rotating crack model. $\sigma_{yy} - \varepsilon_{yy}$ response.

differences. In particular, the elasticity-based rotating crack model and the Rankine plasticity model with kinematic hardening show an almost identical behaviour. The behaviour of the Rankine model with isotropic hardening is identical to the behaviour of the Rankine model with kinematic hardening until the shear stress is equal to zero. At that stage the apex of the yield surface has been reached for the isotropic hardening model and the shear stress is equal to zero.

The limiting case with no softening ($G_f = \infty$) confirms that the different formulations within the total strain concept result in a similar behaviour. The shear stress–shear strain responses of the rotating crack model and the Rankine plasticity model are shown in Figure 8. The response is identical for all models with a total formulation. It is clear from this figure that although no softening has been assumed, the shear stress–shear strain response shows an implicit softening behaviour. Also depicted in Figure 8 is the response of the Rankine model formulated within an incremental concept, which shows a shear stress–shear strain response that is less flexible, but still shows an implicit shear softening. The coincidence between the rotating crack model and the Rankine plasticity model based on the deformation theory for ideal plasticity has also been shown in [13].

The plasticity model based on an incremental formulation has also been applied to the tension-shear model problem with the standard softening material properties and compared with the rotating crack model in the following figures. The first interest concerns the behaviour in shear which is depicted in Figure 9. It is clear from Figure 9 that the rotating crack model has the most flexible response in shear, but the differences between the rotating crack model and the plasticity model are minor. Again, the Rankine plasticity model with isotropic hardening results in a shear stress equal

to zero when the apex of the yield surface has been reached. The normal stress–strain response in the x-direction, Figure 10, again shows an implicit normal stress–shear stress coupling for the models based on an incremental formulation, with an even more pronounced coupling for the plasticity model. The normal stress–normal strain response in the lateral direction, depicted in Figure 11

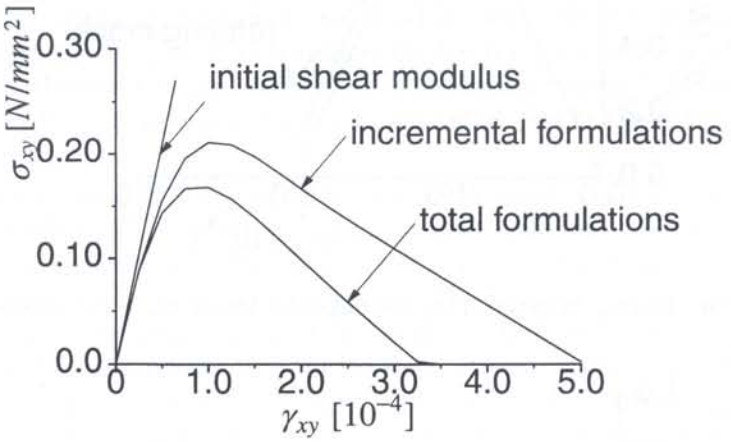

Fig. 8. $G_f = \infty$. $\sigma_{xy} - \gamma_{xy}$ response.

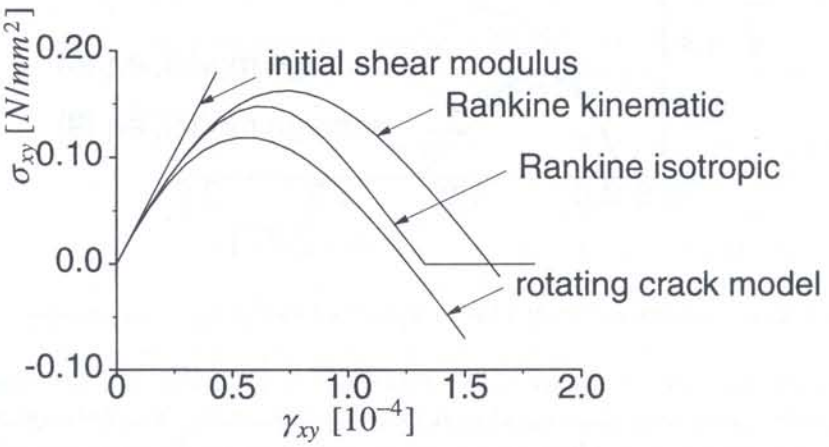

Fig. 9. Tangential formulations and the rotating crack model. $\sigma_{xy} - \gamma_{xy}$ response.

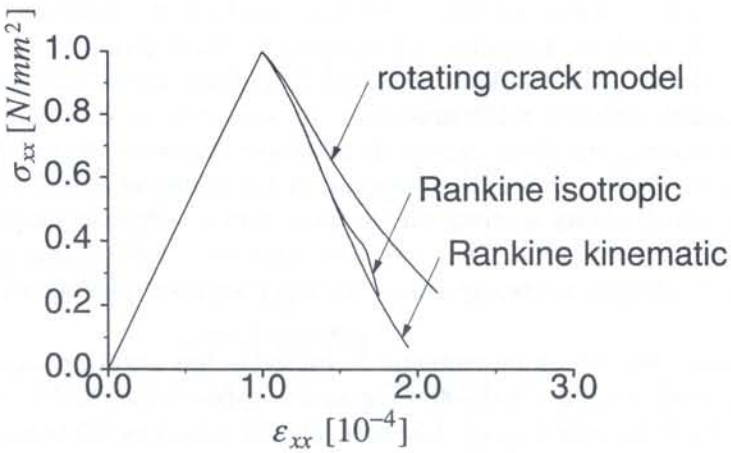

Fig. 10. Tangential formulations and the rotating crack model. $\sigma_{xx} - \varepsilon_{xx}$ response.

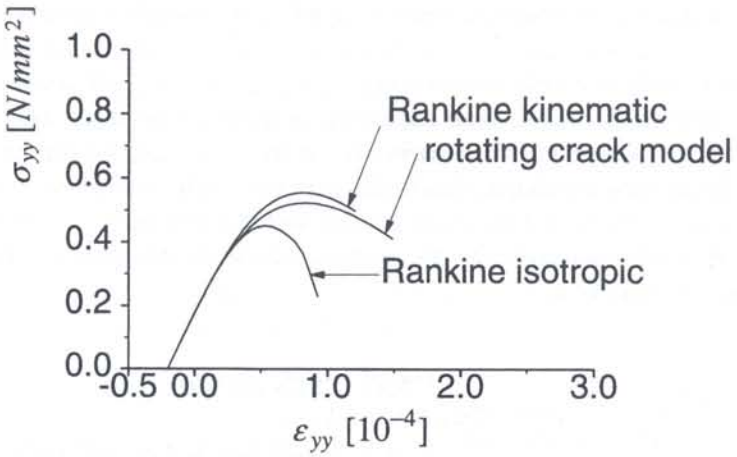

Fig. 11. Tangential formulations and the rotating crack model. $\sigma_{yy} - \varepsilon_{yy}$ response.

shows a similar behaviour as for the models based on the total formulation, given in Figure 7. The response for the Rankine plasticity model with isotropic hardening again shows the linear softening relation when the apex of the yield surface has been reached. The Rankine plasticity model with kinematic hardening shows a gradual degradation of the stiffness in the y-direction.

3.3. Influence of crack models in reinforced concrete

Now, we shall investigate how the differences between the various smeared-crack models that were brought out before for plain concrete carry over to reinforced concrete. This will be done by the analysis of an idealised panel, which can be modelled as a single element [13]. The panel has the dimensions 10×10 mm^2 and has a thickness of 1 mm. It is reinforced with one layer of a reinforcing grid with $\psi = 0°$, Figure 12. The reinforcement ratio in the p-direction is equal to 0.04232 and in the q-direction equal to 0.00768. The Young's modulus of the reinforcement is $E_s = 200,000$ MPa and the yield strength of the steel is $f_{sy} = 500$ MPa. The panel is loaded in a combined biaxial tension-shear loading with $\sigma_{xx} = \sigma_{yy} = 2.5\mu$ MPa and $\sigma_{xy} = 5.0\mu$ MPa, with μ the loading parameter such that it is equal to one at the analytical collapse load associated with yielding of the reinforcement [13]. The analytical collapse load has been determined with a no-tension limit analysis with linear-elastic behaviour in compression (Young's modulus of the concrete $E = 20,000$ MPa).

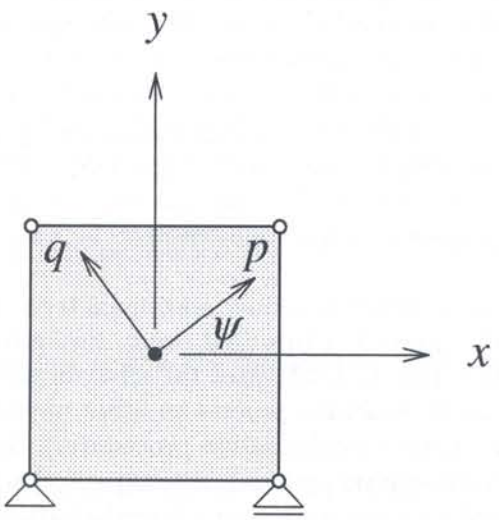

Fig. 12. Finite element model for reinforced concrete panels

The results of the analyses are shown in Figure 13, where the loading parameter is plotted against the x-displacement of the upper-right node of the element. The comparison of the different smeared-crack formulations for plain concrete shows that a proper choice is important even if the tensile strength is equal to zero and a no tension-softening description is used. The interaction between the reinforcement and the concrete compressive struts after cracking results in different responses. The fixed crack model shows a collapse load which is too high, irrespective of the magnitude of the shear retention factor. The rotating crack model and the plasticity-based models approximate the exact failure load. The responses of the rotating crack model and the Rankine deformation plasticity theory are the same [13].

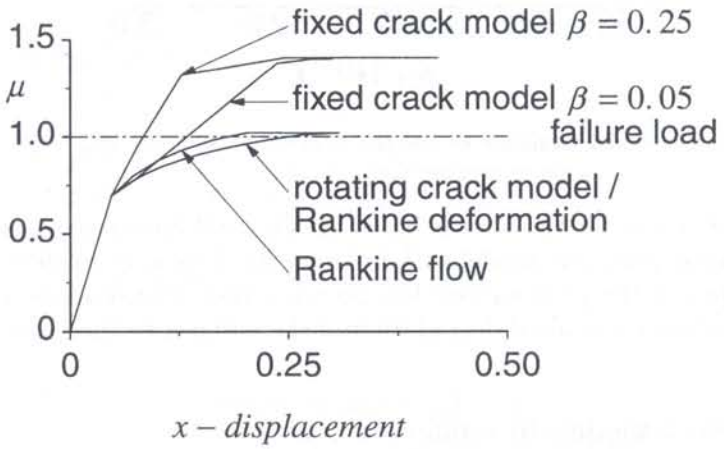

Fig. 13. Results for an idealised reinforced concrete panels

4. Well-posedness of mathematical models

A major problem when using a standard, rate-independent continuum for modelling degradation processes such as smeared cracking is that beyond a certain level of damage accumulation the governing set of partial differential equations changes type. In the static case the elliptic character of the set of partial differential equations is lost, while, on the other hand, in the dynamic case we observe a change of a hyperbolic set into an elliptic set. In both cases the rate boundary value problem becomes ill-posed and numerical solutions suffer from spurious mesh sensitivity.

The inadequacy of the standard, rate-independent continuum to model failure zones correctly is due to the fact that *force–displacement relations* measured in testing devices are simply mapped onto *stress–strain curves* by dividing the force and the elongation by the original load-carrying area and the original length of the specimen, respectively. This is done without taking into account the changes in the micro-structure that occur when the material is so heavily damaged as in fracture processes. Therefore, the mathematical description ceases to be a meaningful representation of the physical reality.

To solve this problem one must either introduce additional terms in the continuum description which reflect the changes in the micro-structure that occur during fracture, or one must take into account the viscosity of the material. In both cases the effect is that the governing equations do not change type during the damage evolution process and that physically meaningful solutions are obtained for the entire loading range (regularisation procedures). It is emphasised that although concrete can be regarded as a disordered material, the introduction of stochastic distributions of defects does not replace the need for the introduction of regularisation procedures [11]. For a proper description of failure in concrete both enhancements are necessary: enrichment of the continuum

by higher-order terms, either in space or in time, and the introduction of the occurrence of material flaws as a stochastic quantity.

Another way to look upon the introduction of additional terms in the continuum description is that the Dirac distributions for the strain at failure are replaced by continuous strain distributions, which lend themselves for description by standard numerical schemes. Although the strain gradients are now finite, they may be very steep and the concentration of strain in a small area can still be referred to as *strain localisation* or *localisation of deformation.*

The essential deficiency of the standard continuum model can be demonstrated simply by the example of a simple bar loaded in uniaxial tension, Figure 14, e.g. [6]. Let the bar be divided into m elements. Prior to reaching the tensile strength f_t a linear relation is assumed between the (normal)

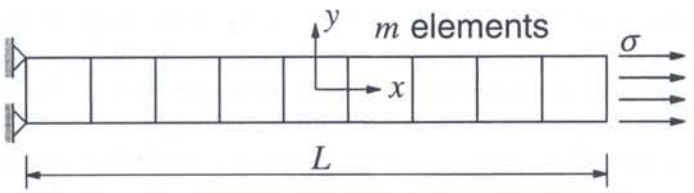

Fig. 14. Strain-softening bar subjected to uniaxial loading

stress σ and the (normal) strain ε:

$$\sigma = E\varepsilon \tag{32}$$

with E Young's modulus. After reaching the peak strength a descending slope is defined in this diagram through an affine transformation from the measured load–displacement curve. The result is given in the left part of Figure 15, where ε_u marks the point where the load-carrying capacity is

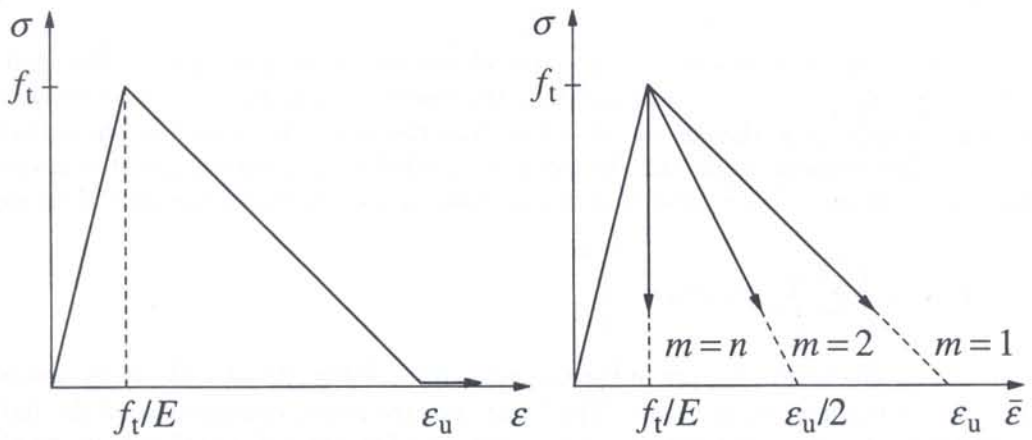

Fig. 15. Stress–strain diagram (left) and response of an imperfect bar in terms of an stress-average curve (right)

totally exhausted. In the post-peak regime the constitutive model can thus be summarised as:

$$\varepsilon = \varepsilon^{e} + \varepsilon^{i}, \tag{33}$$

which constitutes a decomposition of the strain into an elastic part ε^{e}:

$$\varepsilon^{e} = E^{-1}\sigma \tag{34}$$

and a contribution due to inelastic effects (e.g., cracking or plastic slip)

$$\varepsilon^{\mathrm{i}} = h^{-1}(\sigma - f_{\mathrm{t}})\,, \tag{35}$$

where h plays a role for the inelastic strain ε^{i} similar to that of E for the elastic strains. In case of degrading materials $h < 0$. Eq. (35) may also be thought of as an integrated form of the evolution equation for the stress rate after failure:

$$\sigma = f_{\mathrm{t}} + h\varepsilon^{\mathrm{i}}\,. \tag{36}$$

Now suppose that one element has a tensile strength that is marginally below that of the other $m-1$ elements. Upon reaching the tensile strength of this element failure will occur. In the other, neighbouring elements the tensile strength is not exceeded and they will unload elastically. The result on the *average* strain of the bar $\bar{\varepsilon}$ is plotted in the right part of Figure 15 for different discretisations of the bar. The results are fully dominated by the discretisation, and convergence to a "true" post-peak failure curve does not seem to occur. In fact, it does occur, as the failure mechanism in a standard continuum is a line crack with zero thickness. The finite element solution of our continuum rate boundary value problem simply tries to capture this line crack, which results in localisation in one element, irrespective of the width of this element. The result on the load–average strain curve is obvious: for an infinite number of elements ($m \to \infty$) the post-peak curve doubles back on the original loading curve. Numerous numerical examples for all sorts of materials exist which further illustrate the above argument. From a physical point of view the above behaviour is unacceptable and when we adhere to continuum descriptions one must enrich the continuum by adding higher-order terms, either in space or in time, which can accommodate narrow zones of highly localised deformations.

As an intermediate solution between using the standard continuum model and adding higher-order terms the Crack Band Model has been proposed [4], in which the area under the softening curve in the left part of Figure 15 is considered as a material parameter, the so-called fracture energy:

$$G_{\mathrm{f}} = \int \sigma \,\mathrm{d}u = \int \sigma\varepsilon(s)\,\mathrm{d}u\,. \tag{37}$$

When we prescribe the fracture energy G_{f} as an additional material parameter the global load–displacement response can become insensitive to the discretisation. In finite element calculations the crack localises in a band that is one or a few elements wide, depending on the element type, the element size, the element shape and the integration scheme. In Feenstra [14] it is assumed that the width over which the fracture energy is distributed can be related to the area of an element

$$h = \alpha_h \sqrt{A_e} = \alpha_h \left(\sum_{\xi=1}^{n_\xi} \sum_{\eta=1}^{n_\eta} \det(\mathbf{J}) w_\xi w_\eta \right)^{1/2}\,, \tag{38}$$

in which w_ξ and w_η the weight factors of the Gaussian integration rule as it is tacitly assumed that the elements are integrated numerically. The local, isoparametric coordinates of the integration points are given by ξ and η, and $\det(\mathbf{J})$ is the Jacobian of the transformation between the local, isoparametric coordinates and the global coordinate system. The factor α_h is a modification factor which is equal to one for quadratic elements and equal to $\sqrt{2}$ for linear elements [21].

Although the introduction of a fracture energy is a major improvement in calculations using any smeared-crack concept, locally nothing has altered and localisation still takes place in one row of elements. This is logical, since the loss of ellipticity occurs at a local level, even though the energy that is dissipated remains constant by adapting the softening modulus to the element size. For numerical simulations this implies for instance that severe convergence problems are usually encountered if the mesh is refined or if in addition to matrix failure the possibility of interface debonding between matrix and grains is modelled by inserting interface elements in the numerical model [22]. Also, the frequently reported observation still holds that the localisation zones are

biased by the discretisation and tend to propagate along the mesh lines. This can be nicely demonstrated with the example of impact loading of a concrete specimen in a Split–Hopkinson device, Figure 16 [24]. The results for the deformed specimen at failure are shown in Figure 17 for three different discretisations in the region between the notches. We observe a clear spurious localisation pattern with the localisation concentrated in a single band of elements which generally follows the mesh lines and occasionally jumps from one row to the next and back without any physical motivation.

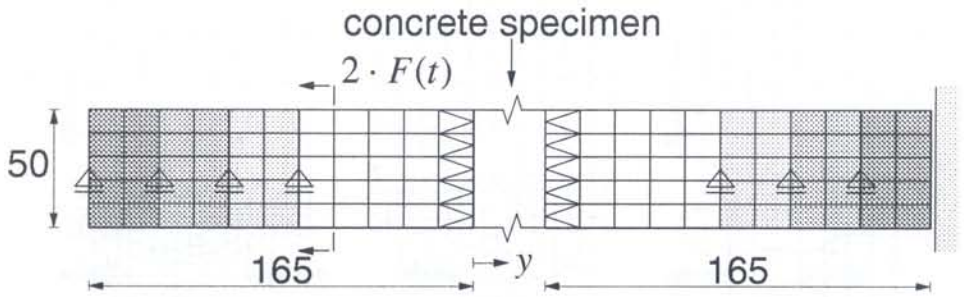

Fig. 16. Numerical model of Split–Hopkinson bar

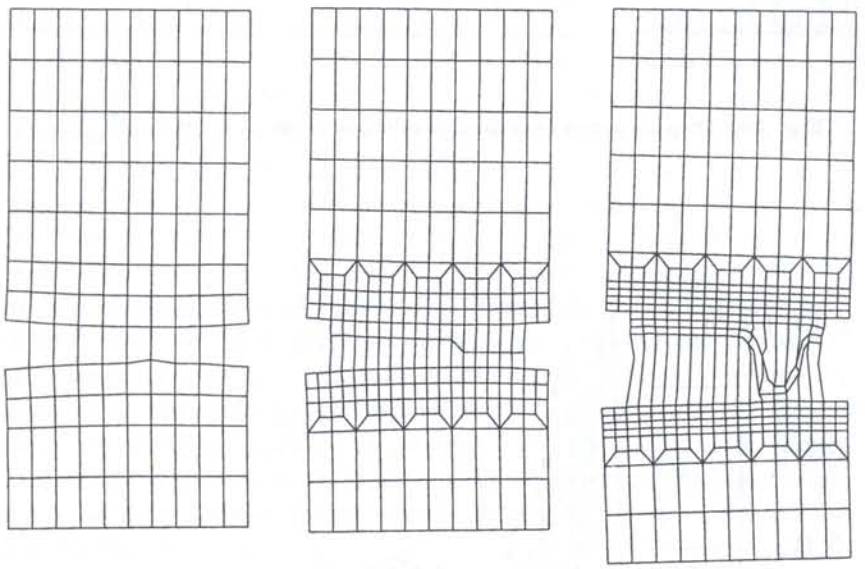

Fig. 17. Displacements of concrete specimen ($t = 0.50 \cdot 10^{-3}$ s)

From a physical point of view the introduction of rate dependence is perhaps the most natural way to regularise ill-posed initial value problems which arise because of the introduction of damage or frictional effects. Here we adopt a simple, linear rate-dependent smeared crack model as developed by Sluys [24]. In it the major principal stress degrades according to

$$\sigma = f_t + h\varepsilon^i + m\frac{\partial \varepsilon^i}{\partial t} \tag{39}$$

with ε^i the inelastic strain, h the softening modulus and m a rate-sensitivity parameter. Using the rate-dependent smeared crack model as defined in Eq. (39) the experiment of a concrete specimen under impact loading in a Split–Hopkinson bar has been reanalysed. The incremental displacement patterns are shown in Figure 18. The most striking difference with the displacement pattern of

Figure 17 is that localisation now does not proceed along the element lines and is no longer confined to the rows of elements between the notches. This is even more obvious when the strains in the vertical direction are plotted (ε_{yy}) as has been done in Figure 19. We observe a clear branching of the cracks.

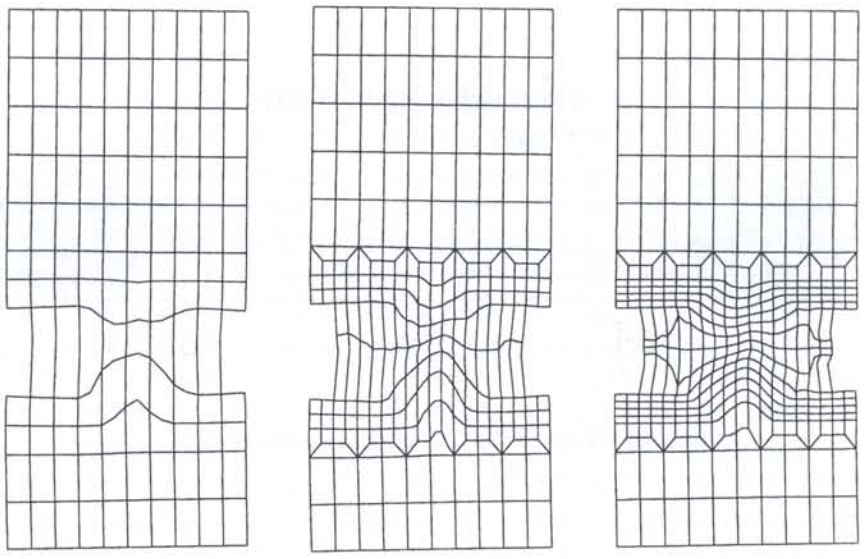

Fig. 18. Displacements for rate-dependent analysis at $t = 0.45 \cdot 10^{-3}$ s

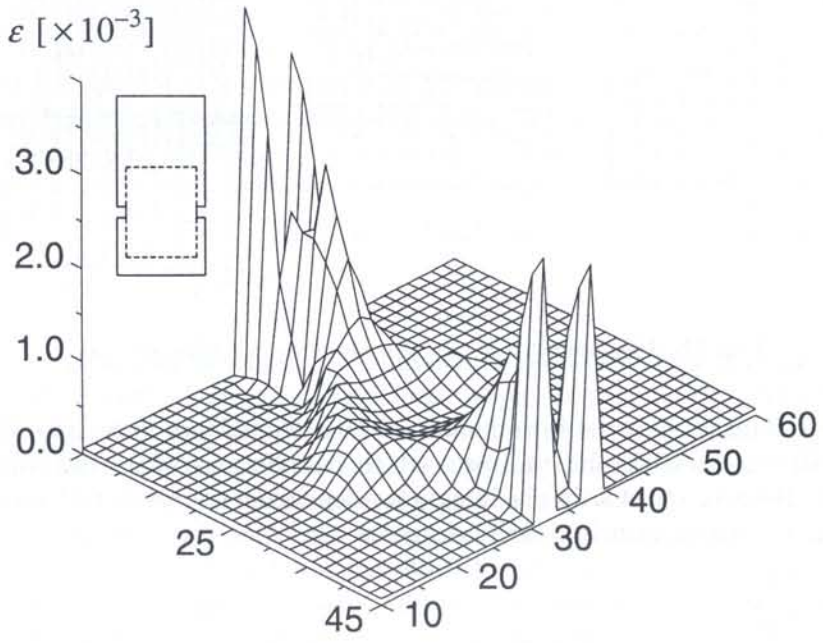

Fig. 19. Axial strain profile in the notched area at $t = 0.45 \cdot 10^{-3}$ s

5. Shortcomings of numerical models

Ever since the landmark paper of Nagtegaal *et al.* [20] researchers have tried to improve finite element concepts such that the observed "locking behaviour" at fully developed plastic flow can be eliminated or at least alleviated. To repeat the problem in simple terms, we refer to the elementary element patch of Figure 20, which is thought as being representative of a large finite element grid if the given boundary conditions are adopted (cf. [17]). For simplicity we have selected simple, constant strain triangles and we have adopted a plane-strain configuration, so that the out-of-plane

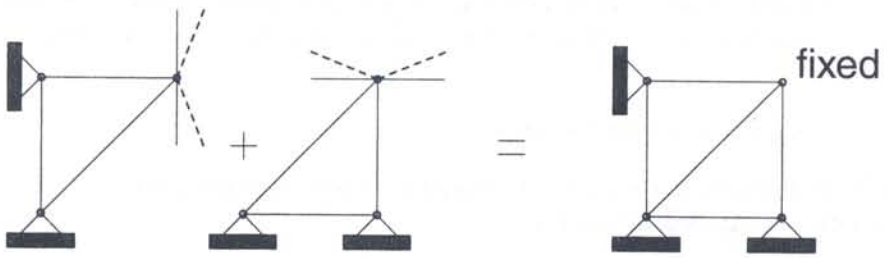

Fig. 20. Locking of two three-noded triangular elements for fully developed plastic flow

strains are zero. Obviously, any constitutive relation that makes the material incompressible, such as incompressible elasticity, or Mises–Huber plasticity at fully developed plastic flow, constrains the movement of the right-upper node to a horizontal line when applying this kinematic constraint to the right-lower element. Similarly, the left-upper element constrains the possible displacement of this node to a vertical line, as also indicated in Figure 20. Evidently, no displacements of the node are possible and an excessively overstiff behaviour is obtained in incompressible elasticity while a severe overestimation of the collapse load is observed in elastoplastic calculations, if a proper limit load can be obtained at all. This phenomenon, which occurs particularly for low-order finite elements in plane strain, axisymmetric and three-dimensional configurations, is now well-known in the literature and an abundance of possible solutions have been put forward. One of the early solutions is the use of special arrangements of elements, such as the crossed triangular patches [20], the use of reduced or selective integration [29], which is closely related to the $\bar{\mathbf{B}}$ approach of [16], the independent interpolation of displacements and pressures [5, 27], where the pressure degrees-of-freedom are usually condensed at element level, the mixed approaches, where especially the Enhanced Assumed Strain concept of Simo and his co-workers [26] has gained much popularity, and finally the use of higher-order displacement models [7, 23], which is maybe the "royal road solution", expensive, but very robust.

While the phenomenon of "element locking" in isochoric deformations has received much attention in the past, it has not been recognised at a large scale that dilatant or contractant plastic flow imposes essentially the same kinematic constraint upon the elements. As will be argued below in a more rigorous manner, plastic dilatancy or contractancy essentially imposes a pointwise relation between the shear deformation and the volumetric deformation. For the constant strain elements of Figure 20 this means that if the right-lower element is sheared, a volumetric strain *must* occur, and the node can only translate along one of the dashed lines emanating from the node, where the amount of uplift is governed by the dilatancy ψ of the material. Similarly, any shearing applied to the other element also causes volumetric straining, and as a result the movements of the same node are restricted to the other set of dashed lines. The conclusion is that, similar to the case of isochoric deformations, which obviously is just a special case ($\psi = 0$), no movement is allowed and no proper collapse load can be obtained for ideal plasticity.

Another problem that has been given less exposure than deserved is the danger that inelastic constitutive relations cause spurious element behaviour. It is known that for instance at ideal plasticity the tangent operator of the constitutive relations has at least one zero eigenvalue. It

turns out that for certain element formulations, especially when reduced integration is applied, or when mixed methods are adopted, the element tangent stiffness may exhibit a multitude of zero eigenvalues, thus leading to highly unstable element behaviour. In practical computations, a premature divergence of the global equilibrium-finding iterative procedure is often observed as a result of this.

5.1. Basic notions in soil plasticity

One of the most frequently used yield criteria for soils and rocks is the over two centuries-old Coulomb criterion. Expressed in terms of principal stresses, the Mohr–Coulomb yield function reads:

$$f = \tfrac{1}{2}(\sigma_3 - \sigma_1) + \tfrac{1}{2}(\sigma_3 + \sigma_1)\sin\phi - c\cos\phi, \tag{40}$$

with ϕ the angle of internal friction, c the cohesion of the material and $\sigma_1 \leq \sigma_2 \leq \sigma_3$. A non-associative flow rule is obtained by adopting

$$\dot{\boldsymbol{\varepsilon}}^{\mathrm{p}} = \dot{\lambda}\frac{\partial g}{\partial \boldsymbol{\sigma}}, \tag{41}$$

with g a plastic potential function that resembles the yield function f:

$$g = \tfrac{1}{2}(\sigma_3 - \sigma_1) + \tfrac{1}{2}(\sigma_3 + \sigma_1)\sin\psi - \text{const.} \tag{42}$$

ψ is an additional material constant, which is commonly named the angle of dilatancy. The angle of dilatancy controls the amount of plastic volume change. Defining the volumetric plastic strain rate as

$$\dot{\varepsilon}_{\mathrm{v}}^{\mathrm{p}} = \dot{\varepsilon}_1^{\mathrm{p}} + \dot{\varepsilon}_2^{\mathrm{p}} + \dot{\varepsilon}_3^{\mathrm{p}} \tag{43}$$

and introducing the rate of plastic shear deformation

$$\dot{\gamma}^{\mathrm{p}} = \dot{\varepsilon}_3^{\mathrm{p}} - \dot{\varepsilon}_1^{\mathrm{p}} \tag{44}$$

one can use Eqs. (41) and (42) to derive that

$$\dot{\varepsilon}_{\mathrm{v}}^{\mathrm{p}} = \dot{\gamma}^{\mathrm{p}}\sin\psi \tag{45}$$

which shows that the angle of dilatancy ψ sets the ratio between the rate of plastic shear deformation and the rate of plastic volume change. For $\psi > 0$ an irreversible increase of volume occurs, while for $\psi < 0$ a decrease is predicted (plastic contraction). $\psi = 0$ is the special case of plastically volume-preserving (isochoric) flow. The Tresca plasticity model with an associative flow rule is obtained by setting $\phi = \psi = 0$ in Eqs. (40) and (42).

5.2. Element locking in dilatant flow

In ideal plasticity, the behaviour at a limit state requires that the stress field remains stationary. In consideration of the injective relation that exists between the stress rate $\dot{\boldsymbol{\sigma}}$ and the elastic strain rate $\dot{\boldsymbol{\varepsilon}}^{\mathrm{e}}$, the elastic strain rates must vanish at this point and relation (45) changes into

$$\dot{\varepsilon}_{\mathrm{v}} = \dot{\gamma}\sin\psi \tag{46}$$

which effectively imposes a kinematic constraint on the possible velocity field. It is emphasised that this constraint condition applies irrespective of the value of ψ, and that $\psi = 0$ (volume-preserving plastic flow) is just a special case. Another case where material behaviour imposes a kinematic constraint upon the velocity field is when a matrix material is reinforced with inextensible fibres.

Now, we choose the principal axes of the strain rate tensor to coincide with the local ξ, η-coordinate system of an element. This choice is permissible, since under planar deformations $\dot{\varepsilon}_v$ and $\dot{\gamma}$ are both invariant. For the Mohr–Coulomb yield function resembling plastic potential (42), Eq. (46) then specialises as

$$(1 - \sin\psi)\dot{\varepsilon}_\xi + (1 + \sin\psi)\dot{\varepsilon}_\eta + \dot{\varepsilon}_\zeta = 0\,. \tag{47}$$

We now consider the four-noded plane strain element of Figure 21. This element configuration can

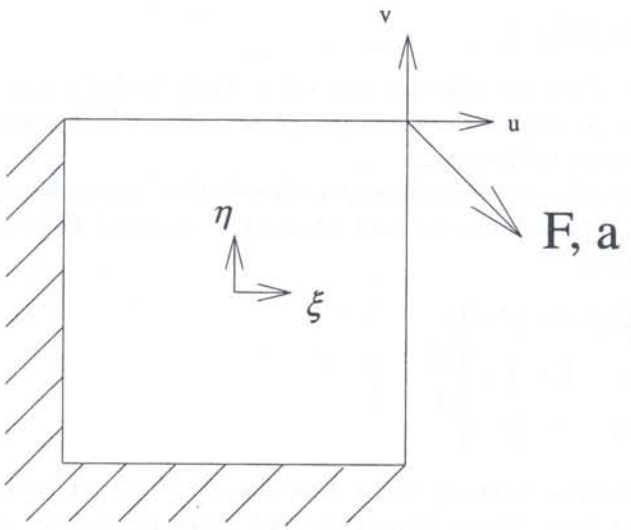

Fig. 21. Single four-noded element subjected to non-uniform shear

be thought of as representative for an arbitrary domain of finite elements with boundary conditions [17]. The velocities within the element are interpolated in a standard isoparametric fashion, so that

$$\begin{aligned} \dot{u} &= \tfrac{1}{4}(1+\xi)(1+\eta)\dot{u} \\ \dot{v} &= \tfrac{1}{4}(1+\xi)(1+\eta)\dot{v} \end{aligned} \tag{48}$$

The normal strain rates within the element are obtained by standard differentiation as:

$$\begin{Bmatrix} \dot{\varepsilon}_\xi \\ \dot{\varepsilon}_\eta \\ \dot{\varepsilon}_\zeta \end{Bmatrix} = \frac{1}{4}\begin{bmatrix} 1+\eta & 0 \\ 0 & 1+\xi \\ 0 & 0 \end{bmatrix} \begin{Bmatrix} \dot{u} \\ \dot{v} \end{Bmatrix}. \tag{49}$$

Upon substitution of expressions (49) for the strain rates into the kinematic constraint (47), the following restriction upon the velocity field ensues:

$$[(1 - \sin\psi)\dot{u} + (1 + \sin\psi)\dot{v}] + (1 - \sin\psi)\dot{u}\eta + (1 + \sin\psi)\dot{v}\xi = 0\,. \tag{50}$$

The term between square brackets sets the ratio between the horizontal velocity $\dot{u}$ and the vertical velocity $\dot{v}$ of the right upper node of the element. Its vanishing is a direct reflection of the kinematic constraint imposed on the possible velocity field by the constitutive relation. Since this term must be zero, vanishing of the entire identity (50) can only be achieved for arbitrary pairs ξ, η if $\dot{u}$ and $\dot{v}$ are both zero. This implies that the element is not able to deform, which phenomenon is known as volumetric locking. We emphasise that this observation holds for all values of ψ, including the isochoric case ($\psi = 0$).

Next we consider the case of uniform reduced integration for the four-noded quadrilateral (one-point integration). For this element, denoted by Qr4 in the remainder of this article, the normal strain rate field is defined as:

$$\begin{Bmatrix} \dot{\varepsilon}_\xi \\ \dot{\varepsilon}_\eta \\ \dot{\varepsilon}_\zeta \end{Bmatrix} = \frac{1}{4} \begin{bmatrix} 1 & 0 \\ 0 & 1 \\ 0 & 0 \end{bmatrix} \begin{Bmatrix} \dot{u} \\ \dot{v} \end{Bmatrix} \tag{51}$$

and substitution of this expression in the kinematic constraint (47) gives:

$$(1 - \sin\psi)\dot{u} + (1 + \sin\psi)\dot{v} = 0\,, \tag{52}$$

which is satisfied by definition for arbitrary pairs ξ, η. Volumetric locking will therefore not occur, but as is well-known, the Qr4 element has two hourglass modes, which makes practical computations not feasible without proper stabilisation.

Thirdly, we consider the four-noded element with selective (one-point) integration on the dilatational strain rate. This approach can be cast within the so-called $\bar{\mathbf{B}}$-concept [16] and the normal strain rates are redefined as

$$\begin{Bmatrix} \dot{\varepsilon}_\xi \\ \dot{\varepsilon}_\eta \\ \dot{\varepsilon}_\zeta \end{Bmatrix} = \frac{1}{4} \begin{bmatrix} 1 + \frac{2}{3}\eta & -\frac{1}{3}\xi \\ -\frac{1}{3}\eta & 1 + \frac{2}{3}\xi \\ -\frac{1}{3}\eta & -\frac{1}{3}\xi \end{bmatrix} \begin{Bmatrix} \dot{u} \\ \dot{v} \end{Bmatrix}. \tag{53}$$

Note that the normal strain rate in the third direction, $\dot{\varepsilon}_\zeta$, does not vanish pointwise, but only in an average sense. Substitution of this strain rate field in the kinematic constraint (47) leads to

$$[(1 - \sin\psi)\dot{u} + (1 + \sin\psi)\dot{v}] - \sin\psi(\dot{u}\eta + \dot{v}\xi) = 0\,. \tag{54}$$

Obviously, this condition can only be satisfied for arbitrary pairs ξ, η when $\psi = 0$, the special case of plastically volume preserving flow. For arbitrary values of ψ, that is for dilatant plastic flow ($\psi > 0$), or contractant plasticity ($\psi < 0$), $\dot{u}$ and $\dot{v}$ must vanish identically, which means that the Q4 $\bar{\mathbf{B}}$ element locks for the general case of $\psi \neq 0$, and is only effective for the case of isochoric plastic flow. This is demonstrated for the elementary test of Figure 21, where a single element is subjected to non-uniform shear. A Drucker–Prager flow rule with an angle of internal friction $\phi = 30^\circ$ and a dilatancy angle of $\psi = 20^\circ$ is adopted. Obviously, the standard four-noded four-noded element locks completely, but also the Q4 $\bar{\mathbf{B}}$ element does not result in a yield plateau, Figure 22. The latter result confirms the conclusion drawn from Eq. (15).

Next, we augment the strain rates by defining additional strain rate fields. The simplest possible enrichment for the normal strain rate field is to set

$$\begin{Bmatrix} \dot{\varepsilon}_\xi \\ \dot{\varepsilon}_\eta \\ \dot{\varepsilon}_\zeta \end{Bmatrix} = \frac{1}{4} \begin{bmatrix} 1 + \eta & 0 \\ 0 & 1 + \xi \\ 0 & 0 \end{bmatrix} \begin{Bmatrix} \dot{u} \\ \dot{v} \end{Bmatrix} + \begin{bmatrix} \xi & 0 \\ 0 & \eta \\ 0 & 0 \end{bmatrix} \begin{Bmatrix} \dot{\alpha}_1 \\ \dot{\alpha}_2 \end{Bmatrix} \tag{55}$$

with $\dot{\alpha}_1$, $\dot{\alpha}_2$ additional, incompatible strain rate variables. Substitution of the strain rate field (55) in the kinematic constraint yields

$$\begin{aligned} &[(1 - \sin\psi)\dot{u} + (1 + \sin\psi)\dot{v}] \\ &+(1 - \sin\psi)\eta(\dot{u} + 4\dot{\alpha}_2) + (1 + \sin\psi)\xi(\dot{v} + 4\dot{\alpha}_1) = 0\,. \end{aligned} \tag{56}$$

which is satisfied for arbitrary pairs ξ, η for

$$(1 - \sin\psi)\dot{u} + (1 + \sin\psi)\dot{v} = 0\,,$$

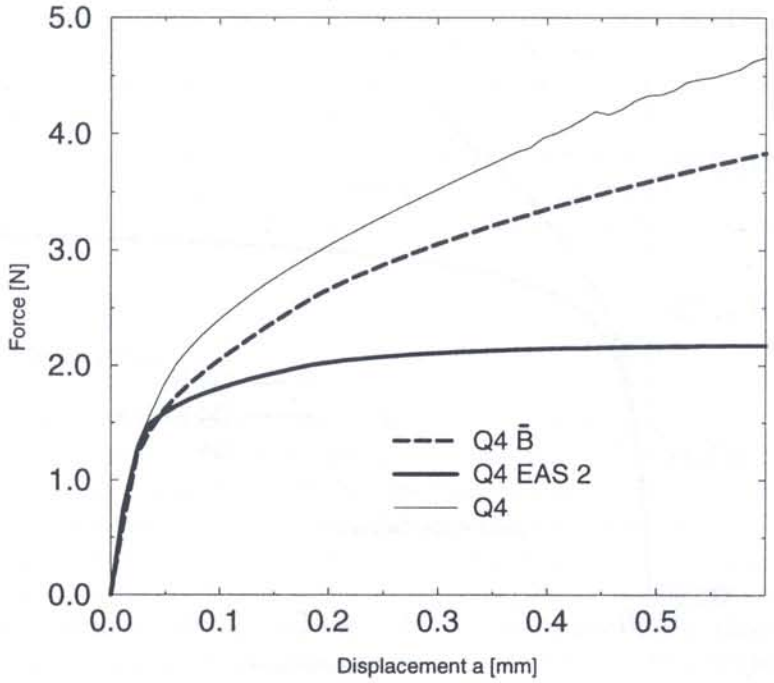

Fig. 22. Force–displacement curves for single four-noded element. Drucker–Prager flow with $\phi = 30°$, $\psi = 20°$

$$\dot{u} + 4\dot{\alpha}_2 = 0\,. \tag{57}$$

$$\dot{v} + 4\dot{\alpha}_1 = 0\,.$$

Accordingly, an element is obtained that is free of volumetric locking effects for *all* values of ψ. This is confirmed by the non-uniform shear test of Figure 21. Figure 22 shows that this element, which will henceforth be called Q4 EAS 2 since two extra variables are used to enrich the strain rate field, indeed captures a proper limit load.

Figure 23 shows the response obtained for a rigid disk which is being pushed into a halfspace. The boundary conditions are such that symmetry conditions apply at the left boundary while the lower and right boundaries are fully restrained. Loading is applied by direct displacement control of the disk. Non-associated Drucker–Prager ideal plasticity is used with a Young's modulus $E = 50$ MPa, a Poisson's ratio $\nu = 0.25$, a cohesion $c = 2$ kPa, a friction angle $\phi = 30°$ and a dilatancy angle $\psi = 10°$ (dilatant flow). The standard Q4 element and — as predicted for dilatant plastic flow — the selectively integrated Q4 element show significant locking. The Q4 EAS 3 element (the axisymmetric version of the Q4 EAS 2 element) captures the limit load properly without giving convergence difficulties. On the other hand, the Q4 EAS 5 element, in which the shear strains are enhanced in addition to the normal strains, originally introduced by Simo and Rifai [26], behaves unstable and diverges in an early stage of the loading process. The reason for this behaviour will be explained next.

5.3. Spurious mechanisms

In non-associated plastic flow without hardening, the elastoplastic tangential matrix reads:

$$\mathbf{D}^{\mathrm{ep}} = \mathbf{D} - \frac{\mathbf{D}\mathbf{m}\mathbf{n}^{\mathrm{T}}\mathbf{D}}{\mathbf{n}^{\mathrm{T}}\mathbf{D}\mathbf{m}} \tag{58}$$

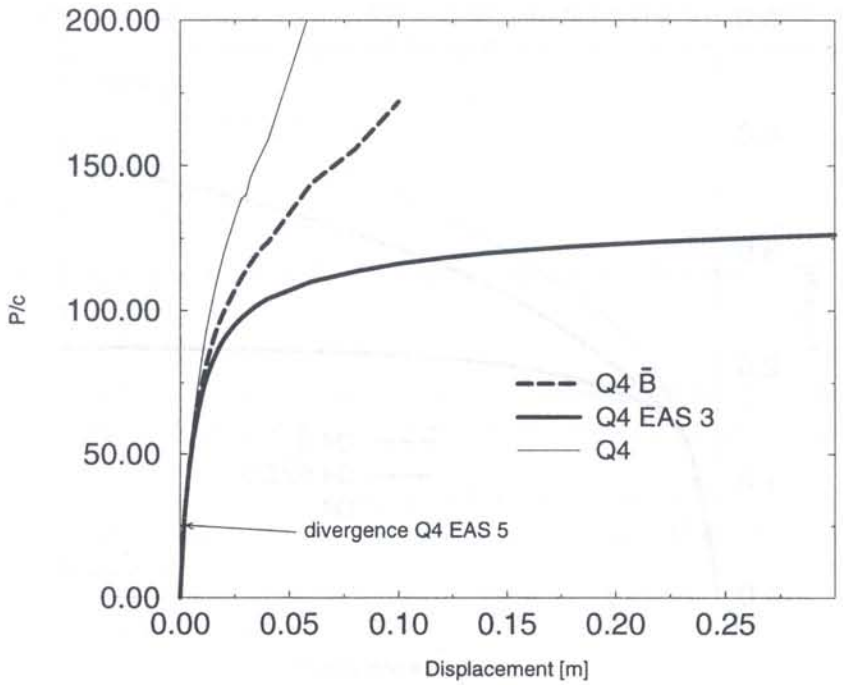

Fig. 23. Load–settlement curve for axisymmetric punch problem

in which $\mathbf{D}$ is the elastic stress–strain matrix, $\mathbf{n} = \partial f/\partial \boldsymbol{\sigma}$ is the normal to the yield surface and $\mathbf{m} = \partial g/\partial \boldsymbol{\sigma}$ is the flow direction. This matrix is singular since $\mathbf{m}$ is an eigenvector associated with a zero eigenvalue.

In mixed approaches variables are introduced additional to the standard displacement degrees-of-freedom. If we assemble the displacement nodal degrees-of-freedom in a vector $\mathbf{a}$ and the additional degrees-of-freedom, which are for instance related to enhanced strain interpolations like in the EAS-concept [26], in the vector $\boldsymbol{\alpha}$, then the tangential stiffness relation can generally be written in the following format:

$$\begin{bmatrix} \mathbf{K} & \boldsymbol{\Gamma} \\ \boldsymbol{\Upsilon} & \mathbf{Q} \end{bmatrix} \begin{Bmatrix} \dot{\mathbf{a}} \\ \dot{\boldsymbol{\alpha}} \end{Bmatrix} = \begin{Bmatrix} \mathbf{f}_{\mathrm{a}} \\ \mathbf{f}_{\alpha} \end{Bmatrix} \tag{59}$$

in which $\mathbf{K}$, $\boldsymbol{\Upsilon}$, $\boldsymbol{\Gamma}$ and $\mathbf{Q}$ are submatrices of the total tangential stiffness matrix, and $\mathbf{f}_{\mathrm{a}}$ and $\mathbf{f}_{\alpha}$ are the right-hand side vectors related to the displacement and additional degrees-of-freedom respectively. The superimposed dots denote differentiation with respect to a (virtual) time.

Generally, the additional degrees-of-freedom are condensated at element level. This implies that the condensed element tangential stiffness matrix $\mathbf{K}^* = \mathbf{K} - \boldsymbol{\Gamma}\mathbf{Q}^{-1}\boldsymbol{\Upsilon}$ enters the global or structural tangent stiffness matrix. This tangential stiffness matrix can become singular because of two reasons. Firstly, for ideal plasticity the submatrix $\mathbf{Q}$ can become singular at fully developed plastic flow. As a consequence the condensed tangential stiffness matrix $\mathbf{K}^*$ is undefined. As $\mathbf{K}^*$ is used to assemble the total tangential stiffness matrix, this has a disastrous effect on the total tangential stiffness matrix and thus on the convergence of the global iteration process. For instance, for the five-parameter EAS plane strain/stress element as formulated by Simo and Rifai [26], exact integration yields a non-singular $\mathbf{Q}$-matrix, but a standard 2×2 Gauss integration renders $\mathbf{Q}$ singular. For the seven-parameter assumption of Andelfinger and Ramm [2] singularity of $\mathbf{Q}$ is obtained even for exact integration [15].

The fact that condensation can be performed is a necessary condition for robustness of the element. A second requirement is that the element does not possess spurious mechanisms due to ideal plasticity. In ideal plasticity the elastoplastic material tangential stiffness matrix $\mathbf{D}$ has exactly one zero eigenvalue at smooth parts of the yield surface as has been shown above. Additional

eigenvalues arise in the condensed element tangential stiffness $\mathbf{K}^*$ due to the additional strain rate modes and will result in spurious mechanisms, which are not resisted by surrounding elements.

Similar arguments can be raised for axisymmetric or three-dimensional configurations. Whenever additional fields are introduced for the shear strain rates, spurious mechanisms or worse, breakdown of the condensation mechanism, arise in ideal plastic flow. Finally, it is noted that the occurrence of spurious mechanisms is by no means restricted to mixed appoaches. For the eight-noded quadrilateral element with 2×2 Gaussian integration this has been shown before by de Borst [6].

5.4. Some further comments

The issue of element performance in inelastic solids is still a relatively open area. Pure displacement based elements generally provide the most robust solution in terms of stability of the numerical process. However, especially simple elements like the four-noded element in plane stress/strain and axisymmetric applications and the eight-noded brick element in three-dimensional configurations tend to suffer from diseases as "locking" and poor representation of shear stress in bending. Higher-order interpolations are a possible solution, for instance the fifteen-noded triangle [7, 23] in planar and axisymmetric applications, or the fourteen-noded brick element [25] in three-dimensional situations. However, these elements tend to generate large bandwidths, which leads to relatively large computer times, although this disadvantage gradually diminishes with the rapid increase of computer power. Other solutions, like mixed approaches or reduced/selective integration can be highly efficient, but must be used with care because of the inherent danger of the occurrence of spurious mechanisms in case of inelasticity. It seems that for a successful use of these approaches one must tailor the element to the application.

6. Inadequacies in structural modelling

At the hand of the example of a three-span, skewed-slab bridge, for which *predictive* finite element analyses were carried out prior to its destruction, the importance and the difficulties of adopting proper boundary conditions in numerical analyses will now be illuminated.

6.1. Description of the bridge

The bridge which has been analysed and tested is a three-span, skewed-slab bridge, Figure 24, see also Reference [1], which provides the necessary details on the lay-out of the reinforcement. Inspection prior to the analyses and the testing revealed that severe damage had occurred, especially near the sides of the bridge [1], while the driving lanes were in a reasonable condition. In the areas of visible damage of the concrete the reinforcing bars had corroded severely. The visual inspection was hampered by the existing asphaltic overlay, which was removed only shortly before the final destructive testing.

To obtain a better judgement of the concrete properties cores were drilled at several places. The concrete test specimens were then subjected to uniaxial compression tests which resulted in values for the mass density ρ and for the uniaxial compressive strength f_c which ranged from 2450 kg/m^3 to 2470 kg/m^3 and from 49 MPa to 56 MPa respectively. The value for Young's modulus E appeared to be around 33,000 MPa. As will be detailed below, in the analyses the possible effect on the remaining structural capacity of the observed poor quality of the concrete was modelled by adopting artificially low values for Young's modulus and for the uniaxial compressive strength. Properties for the reinforcing steel could be derived from uniaxial tension tests on rebars [1].

Prior to the final destruction test modal tests were carried out in order to obtain data on the boundary conditions which would have to be applied in the analyses. In contrast to the final

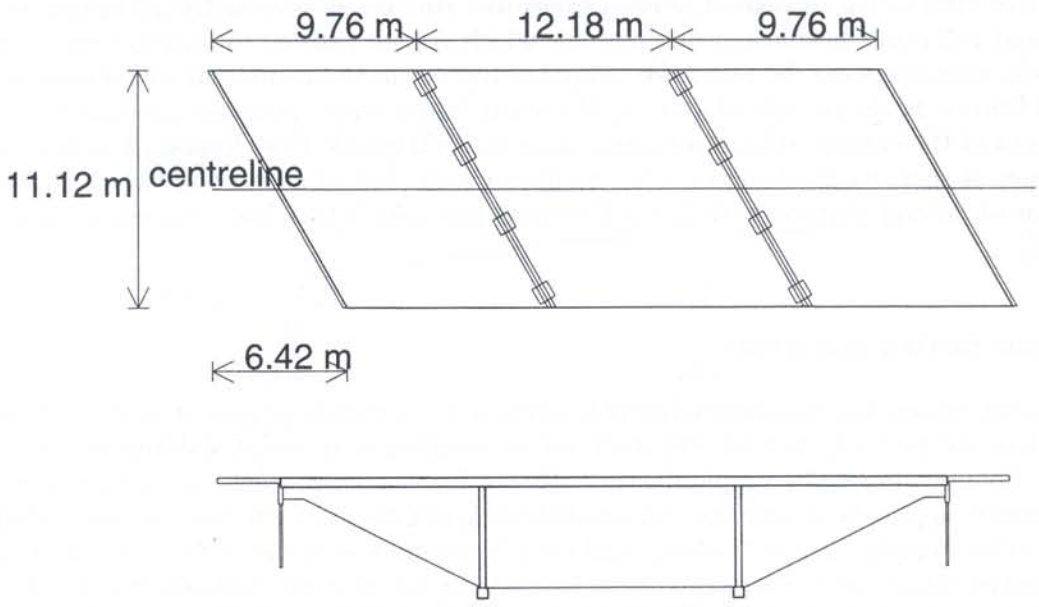

Fig. 24. Plan view and side view of the bridge

destruction test the modal tests were conducted with the asphaltic layer still in place, and resulted in a lowest eigenfrequency of approximately 8.3 Hz [1].

The actual destructive tests were carried by pulling down two concrete blocks of 0.6 m by 1.8 m, which were placed on the bridge deck in order to distribute the forces exerted by servo-controlled hydraulic actuators. On each block two of such actuators were placed. Rock anchors were attached to the actuators to provide the reaction force that was needed to load the bridge. The total load at which failure occurred was 3.24 MN. In the remainder of this article we shall always refer to the load that was exerted on one of the blocks only, so that collapse occurs at a load level of 1.62 MN.

6.2. Discretisation and loading configuration

The finite element mesh that was adopted in the analyses which have been carried out is shown in Figure 25. It consists of 144 eight-noded degenerated plate/shell elements with a 2×2 Gauss

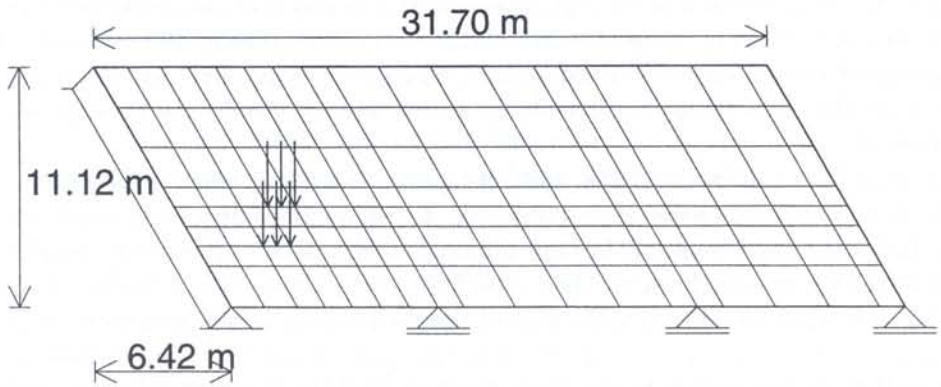

Fig. 25. Finite element model for the Delft FE analysis of the bridge and position of the loads

integration in the plane and a nine-point Simpson integration through the depth. It is noted that the used element may not be optimal for skewed meshes as used here. Reinforcement was modelled using an embedded approach, that is the interpolation functions of the concrete were used also for the reinforcement. The reinforcement grid has its own integration stations, which do not have to coincide with the layers of the plate/shell element. The discretisation of Figure 25 was considered sufficiently refined for the expected bending-type failure. Analyses with different meshes should have been tried to verify this, but, because of time restrictions — the analyses had to be completed before the actual bridge testing — this has not been done. The loading blocks have been modelled as two line loads which were each placed at the edges of two elements, Figure 25. Linear dependence relations have been supplied to ensure that all nodes beneath a line load had the same vertical displacements.

6.3. Assessment of the boundary conditions

The piers have not been modelled in the predictive analyses, because they have no influence on the final collapse load or the failure pattern. However, there is some influence on the load–deflection pattern, not only because of the neglected axial stiffness of the piers, but also because the piers act as rotational springs on the bridge deck. From a hand calculation it appeared that the maximum axial shortening of the piers would be approximately 0.1 mm, which is negligible. The rotational stiffness of the piers was not taken into account either. This simplification will be justified below.

A most important issue when modelling an existing structure is the interaction of the structure with the environment. At the abutments as well as at the piers we have the question whether the most appropriate boundary condition would be a clamped support, a hinged support, or a roller support. The question of clamped support vs. hinged support can be partly resolved by carrying out eigenvalue analyses and comparing the numerical results with the lowest eigenfrequency that comes out of the modal test ($\approx$ 8.3 Hz). In the finite element analyses with the mesh of Figure 25 the mass density of the concrete was taken as $\rho = 2370$ kg/m^3 and Young's modulus E and Poisson's ratio were assumed as 24,800 MPa and 0.2 respectively. The reduced value for Young's modulus was adopted to model the observed deterioration of the concrete. In the first analyses all supports were assumed to be hinged. When the influence of the asphaltic concrete cover was neglected an eigenfrequency of 7.43 Hz was computed, whilst the slightly lower value of 6.76 Hz was found for the analysis in which the asphaltic concrete cover was included. These values are much closer to the experimentally determined eigenfrequency than the value of 22.69 Hz that was obtained for the case with clamped ends and hinged supports at the piers. This indicates that (i) the supports at the abutments are not clamped and (ii) neglecting the bending stiffness of the piers is reasonable. However, the issue of hinged vs. roller supports cannot be answered by modal analyses and will be investigated below.

6.4. Model parameters for nonlinear finite element analysis

In the nonlinear analyses the following data have been used. For the reinforcement an elastic-plastic model was utilised with a Young's modulus $E_s = 200,000$ MPa, an initial yield strength $\sigma_{sy} = 345$ MPa and a hardening modulus $h = 7000$ MPa, which is in agreement with the experimentally supplied data. The inelastic behaviour of concrete in tension has been modelled by the multiple fixed crack model of de Borst and Nauta [8–10] and Rots [21]. The shear retention factor β was set equal to 0.2 in all analyses. For the expected type of bending failure a variation of β hardly has any impact on the results.

To account for the stiffness of the concrete between the smeared-out cracks a tension-stiffening model was adopted with a linear softening branch and an ultimate strain at which the residual load-carrying capacity is exhausted $\varepsilon_u = \frac{1}{2} f_{sy}/E_s$. The factor $\frac{1}{2}$ has been introduced because previous experience has shown that this generally leads to a better prediction of the structural behaviour

and because a hand calculation for a rectangular cross-section showed that taking $\varepsilon_u = f_{sy}/E_s$ would result in a moment at which the steel starts yielding, M_{sy}, that is larger than the moment at which collapse ultimately occurs (M_u).

The concrete stresses in biaxial compression were limited by a Drucker–Prager yield contour, which was fitted such that the pure biaxial compressive strength f_{bc} equals 1.16 times the uniaxial compressive strength f_c. Perfectly plastic behaviour was assumed thereafter, because any introduction of softening in compression would result in an extreme mesh sensitivity, which cannot yet be modelled properly. The uniaxial compressive strength f_c itself was set equal to 27.5 MPa. This is a relatively low value, and was adopted to account for observed damage in the concrete. The tensile strength was initially set equal to $f_t = 3.2$ MPa, which is the value that had been suggested by investigators of the University of Cincinnati [1], but later the value $f_t = 1.8$ MPa has been used which follows from applying $f_t = 0.75(1 + f_c/20)$, which formula is used in the Dutch Codes of Practice. In parameter studies it later appeared that the tensile strength affects the load-deflection curve only in the first stages of cracking.

6.5. Numerical results

When carrying out nonlinear finite element analyses it is sensible to first concentrate on the most important causes of the nonlinear structural behaviour. For 90% of all reinforced concrete structures cracking and yielding of the reinforcement are the dominant nonlinear phenomena which govern the structural response. Therefore, first analyses were carried out in which concrete plasticity was not taken into account. The results are the upper and lower curves of Figure 26, in which half of the total load has been plotted against the deflection of the outermost loading block. The upper curve was obtained under the assumption that all supports (at the abutments and at the piers) were hinges, while the lowermost curve was obtained assuming that all supports were rollers except for one of the abutments.

We observe that this variation in boundary conditions has a tremendous impact on the structural response of the bridge. This phenomenon can be explained as follows. In the latter case (the lower-bound solution) cracks due to the bending moments penetrate deep into depth of the slab which causes large horizontal strains in the midplane of the slab. As a consequence an axial elongation of the midplane occurs. On the other hand, this elongation is entirely prevented in case of hinges at all supports. This means that additional in-plane forces prestress the slab. These membrane forces

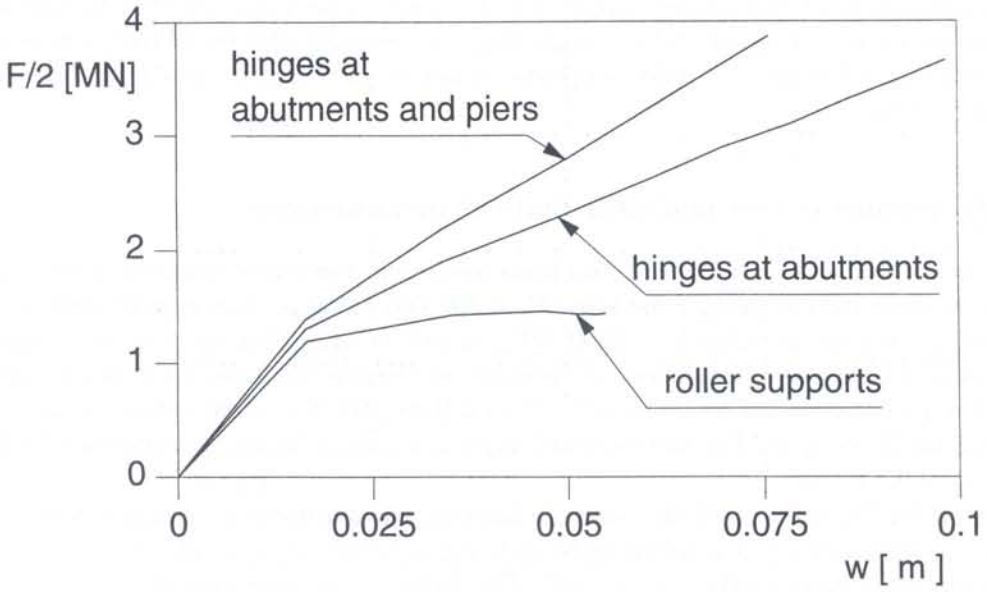

Fig. 26. Influence of boundary conditions on load-bearing capacity

effectively prevent collapse of the bridge, as an almost linearly ascending load–displacement curve was computed up to a displacement of 0.2 m, at which point the calculations were stopped. At this point a large part of the reinforcement was yielding. Because no real collapse load could be identified at this point, which is far beyond the failure loads predicted by yield line solutions [1], the role of the membrane forces seems unrealistically high for these boundary conditions.

To further illustrate the important role of the membrane forces an additional analysis was undertaken in which the piers were roller-supported, but where both abutments were modelled as hinges. The membrane actions that develop are now distributed over all three spans and, as a result, the load–displacement curve nicely falls between both extremes. At a deflection of 0.2 m significant yielding of the reinforcement was again observed, but there were no signs of impending collapse.

The solutions with hinges at all supports and with hinges at only one abutment can be considered as upper and lower bound solutions respectively. Because the precise boundary conditions were unknown a more accurate prediction of the collapse load could only be obtained by improving the upper and lower bounds. To this end the various material data were varied extensively. This appeared to have hardly any impact upon the lower bound solution, but inclusion of concrete plasticity in compression with $f_c = 27.5$ MPa lowered the upper bound solution by about 25%.

6.6. Discussion

The lower bound solution was expected to be closer to the experiment than the upper bound solution, since it was believed that the abutment was not sufficiently rigid to sustain the large horizontal forces without undergoing horizontal displacements. Accordingly, the most realistic assumption for the conditions at the abutments would be roller supports rather than hinges. This expectation was confirmed when the testing had been carried out, Figure 27.

Although the numerically predicted lower-bound solution for the failure load and the experimentally obtained collapse load agree extremely well, this is not completely the case for the failure mechanism. From observations on the experimental failure pattern it seems that first a pure bending type failure has occurred, but that after significant deformations the shear capacity was exhausted. This point, that is when the capacity to sustain external loads starts to decrease, is marked by the onset of the softening branch in Figure 27. Obviously, the used plate/shell element cannot be used to properly model this descending branch where ultimate failure is due to punching.

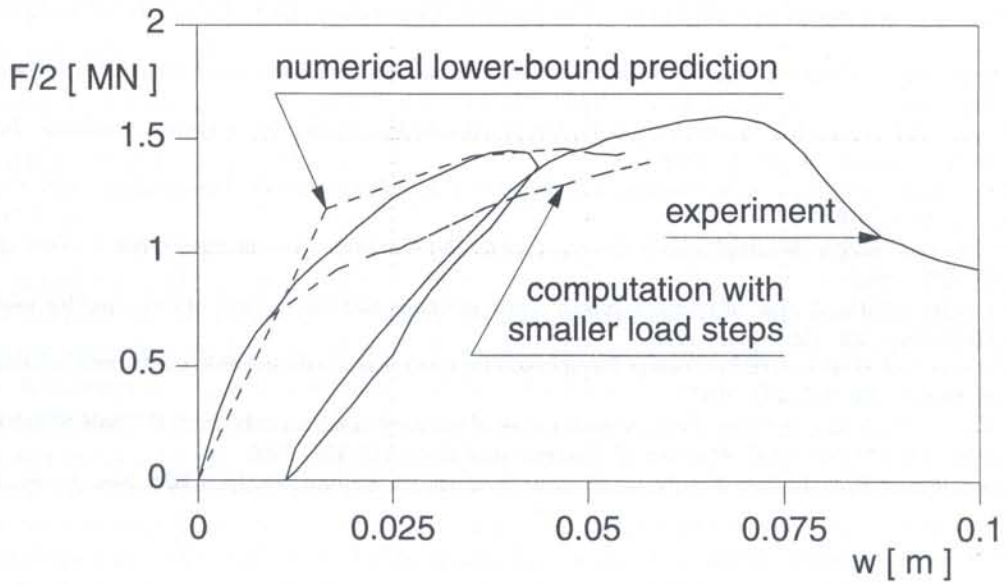

Fig. 27. Numerically obtained lower-bound solution and experimental failure load

REFERENCES

[1] A.E. Aktan, R. Miller, B. Shahrooz. *Destructive field testing of a r/c slab bridge and associated analytical correlation studies.* Research Status Report, University of Cincinnati, Cincinnati, 1991.

[2] U. Andelfinger, E. Ramm. EAS-elements for 2D, 3D, plate and shell structures and their equivalence to HR elements. *Int. J. Num. Meth. Eng.*, **36**: 1311–1337, 1991.

[3] Z.P. Bazant. Comment on orthotropic models for concrete and geomaterials. *ASCE J. Eng. Mech.*, **109**: 849–865, 1983.

[4] Z.P. Bazant, B. Oh. Crack band theory for fracture of concrete. *RILEM Mater. Struct.*, **16**: 155–177, 1983.

[5] P.A.J. van den Bogert, R. de Borst, G.T. Luiten, J. Zeilmaker. Robust finite elements for 3D analysis of rubber-like materials. *Engng. Comput.*, **8**: 3–17, 1991.

[6] R. de Borst. Calculation of collapse loads using higher order elements. In: P.A. Vermeer, H.J. Luger, eds., *IUTAM Symposium on Deformation and Failure of Granular Materials*, 503–513. Balkema, Rotterdam, 1982.

[7] R. de Borst, P.A. Vermeer. Possibilities and limitations of finite elements for limit analysis. *Geotechnique*, **34**: 199–210, 1984.

[8] R. de Borst, P. Nauta. Non-orthogonal cracks in a smeared finite element model. *Engng. Comput.*, **2**: 35–46, 1985.

[9] R. de Borst. *Non-linear analysis of frictional materials.* Dissertation, Delft University of Technology, Delft, 1986.

[10] R. de Borst. Smeared cracking, plasticity, creep and thermal loading — A unified approach. *Comp. Meth. Appl. Mech. Eng.*, **62**: 89–110, 1987.

[11] J. Carmeliet, R. de Borst. Stochastic approaches for damage evolution in standard and non-standard continua. *Int. J. Solids Structures*, **32**: 1149–1160, 1995.

[12] R.J. Cope, P.V. Rao, L.A. Clark, P. Norris. Modelling of reinforced concrete behaviour for finite element analysis of bridge slabs. In: C. Taylor, E. Hinton, D.R.J. Owen, eds., *Numerical Methods for Non-Linear Problems*, Vol. 1, 457–470. Pineridge Press, Swansea, 1980.

[13] M.A. Crisfield, J. Wills. Analysis of R/C panels using different concrete models. *ASCE J. Eng. Mech.*, **115**: 578–597, 1989.

[14] P.H. Feenstra. *Computational aspects of biaxial stress in plain and reinforced concrete.* Dissertation, Delft University of Technology, Delft, 1993.

[15] A.E. Groen. *Improvement of low order elements using assumed strain concepts.* Report 25.2.94.203, Delft University of Technology, Delft, 1994.

[16] T.J.R. Hughes. Generalization of selective integration procedures to anisotropic and nonlinear media. *Int. J. Num. Meth. Eng.*, **15**: 1413–1418, 1980.

[17] T.J.R. Hughes. *The Finite Element Method.* Prentice-Hall, Englewood Cliffs, New Jersey, 1987.

[18] J. Lemaitre, J.L. Chaboche. *Mechanics of Solid Materials.* Cambridge University Press, Cambridge, 1990.

[19] J. Mazars, G. Pijaudier-Cabot. Continuum damage theory — application to concrete. *ASCE J. Eng. Mech.*, **115**: 345–365, 1989.

[20] J.C. Nagtegaal, D.M. Parks, J.R. Rice. On numerically accurate finite element solutions in the fully plastic range. *Comp. Meth. Appl. Mech. Eng.*, **4**: 153–177, 1974.

[21] J.G. Rots. *Computational modeling of concrete fracture.* Dissertation, Delft University of Technology, Delft, 1988.

[22] J.C.J. Schellekens. *Computational strategies for composite structures.* Dissertation, Delft University of Technology, Delft, 1992.

[23] S.W. Sloan, M.F. Randolph. Numerical prediction of collapse loads using finite element methods. *Int. J. Num. Anal. Meth. Geomech.*, **6**: 47–76, 1982.

[24] L.J. Sluys. *Wave propagation, localisation and dispersion in softening solids.* Dissertation, Delft University of Technology, Delft, 1992.

[25] I.M. Smith, D.J. Kidger. Elastoplastic analysis using the 14-node brick element family. *Int. J. Num. Meth. Eng.*, **35**: 1263–1275, 1992.

[26] J.C. Simo, M.S. Rifai. A class of mixed assumed strain methods and the method of incompatible modes. *Int. J. Num. Meth. Eng.*, **29**: 1595–1638, 1990.

[27] T. Sussman, K.-J. Bathe. A finite element formulation for nonlinear incompressible elastic and inelastic analysis. *Comput. Struct.*, **29**: 357–409, 1987.

[28] K. Willam, E. Pramono, S. Sture. Fundamental issues of smeared crack models. In: S.P. Shah, S.E. Swartz, eds., *Proc. SEM/RILEM Int. Conf. Fracture of Concrete and Rock*, 142–157, 1986.

[29] O.C. Zienkiewicz, R.L. Taylor. *The Finite Element Method, 4th Edition.* McGraw-Hill, New Jersey, 1989.